

Galaxies in the Zone of Avoidance

An Infrared Study of HI Detections

Wendy Williams
NASSP Honours
Department of Astronomy, UCT

*Submitted in partial fulfilment of the requirements for the B.Sc (Hons) degree
as part of the National Astrophysics and Space Science Program*

October 2008

Supervisor: P. A. Woudt

Abstract

In this project we study the near infrared (NIR) properties of four galaxies detected in the HI Parkes deep Zone of Avoidance survey (Henning et al., 2005). The NIR J , H and K_s band images have been obtained with the InfraRed Survey Facility (IRSF) in Sutherland which provides better resolution and depth compared to 2MASS (Strutskie, 2006). Magnitudes in all three NIR bands are derived and the extinction obtained by fitting a model Spectral Energy Distribution. The extinction-corrected galaxy colours and apparent magnitudes are determined, the values of which are within the bounds for spiral galaxies.

We fit the radial surface brightness profiles of these spiral galaxies with exponential profiles to obtain the disk scale lengths and central surface brightness. The scale lengths are within the range for typical spirals. From the K_s -band luminosity we estimate the stellar mass and compare this to the HI mass. A comparison to 2MASS results, where available, is also performed.

This project demonstrates the usefulness of NIR imaging and its complementary nature to HI data. Furthermore, it has shown the feasibility of using the NIR images to obtain useful parameters of these highly obscured galaxies.

Acknowledgements

I am grateful to my supervisor, Dr Patrick Woudt, for his support and guidance with this project. I would also like to express my sincere gratitude to Michelle for her help, in particular with SEDs and with lots of other little things. I am thankful for the input of Dr Tom Jarrett regarding my preliminary results and to Prof. Kraan-Korteweg for her comments and suggestions. Thanks also to everyone in the Astronomy department, your support and encouragement is greatly appreciated. Finally, thanks to Kosma and Christina, my classmates and “office”-mates, for insightful conversations and moral support!

I would also like to acknowledge the National Astrophysics and Space Science Program (NASSP) and the National Research Foundation (NRF) for funding this year.

Contents

1	Introduction	1
1.1	Astronomy in the Zone of Avoidance	1
1.1.1	Multiwavelength Surveys	2
1.1.2	Motivation for NIR Follow-up Studies	4
1.2	Extinction	5
1.2.1	Extinction Laws	5
1.2.2	Extinction Maps	6
1.2.3	Internal Extinction	6
1.3	Spectrophotometric Galaxy Modelling	7
1.3.1	GRASIL code	7
1.3.2	SED extinction fitting	8
1.4	Outline	8
2	Observations and Data Reduction	11
2.1	Near Infrared Observations	11
2.1.1	Dithering	12
2.1.2	Flat-fielding and Dark Subtraction	12
2.1.3	Sky Subtraction	12
2.2	Target Selection	13
2.3	IRSF Observations	13
2.4	Data Reduction	14
2.4.1	SIRIUS Pipeline	14
2.4.2	Images	14
2.4.3	Magnitude Zero-Points	16
2.4.4	Photometry	16
3	Data Analysis	21
3.1	Photometric Corrections	21
3.1.1	k -correction	21
3.1.2	Extinction Correction	22
3.2	Spectral Energy Distributions	23

3.2.1	Extinction Fitting	23
4	Results and Discussion	27
4.1	Internal Extinction Estimate	27
4.2	NIR Properties of Selected Galaxies	28
4.2.1	Extinction and k -corrected Magnitudes and Colours	28
4.2.2	Disk Fitting	29
4.2.3	NIR Derived Parameters	33
4.2.4	J0731-27	34
4.3	2MASS Counterparts	35
4.3.1	Comparison	35
5	Conclusion	39
5.1	Summary of Results	39
5.2	Future Prospects	40
A	HI Spectra	41
B	HI Lists	45

List of Figures

1.1	Comparison of 2MASS and IRSF	4
1.2	Model SEDs	8
2.1	Galaxy images	15
2.2	Surface brightness profiles: J0740-22	18
2.3	Surface brightness profiles: J0741-30A	18
2.4	Surface brightness profiles: J0731-27	19
2.5	Surface brightness profiles: J0731-27	19
3.1	NIR-SED: J0740-22	25
3.2	NIR-SED: J0741-30A	25
3.3	NIR-SED: J0731-27	26
3.4	NIR-SED: J0730-28	26
4.1	Correlation of internal extinction and inclination	28
4.2	Exponential disk: J0740-22	31
4.3	Exponential disk: J0741-30A	31
4.4	Exponential disk: J0731-27	32
4.5	Exponential disk: J0731-27	32
4.6	HI mass versus stellar mass	34
4.7	IRSF image of J0731-27	35
4.8	2MASS comparison for J0740-22	36
4.9	2MASS comparison for J0741-30A	36
4.10	2MASS comparison for J0730-28	37
A.1	HIZOA spectrum for J0740-22	41
A.2	HIZOA spectrum for J0741-30A	42
A.3	HIZOA spectrum for J0731-27	43
A.4	HIZOA spectrum for J0730-28	44

List of Tables

2.1	HI properties of sample galaxies	14
2.2	Photometry apertures	17
2.3	NIR surface brightness limits	20
2.4	NIR magnitudes	20
3.1	Extinction in J , H , K_s and V	24
4.1	Internal extinction estimates	27
4.2	Corrected NIR magnitudes and fluxes	29
4.3	NIR colours	29
4.4	Disk scale heights	30
4.5	Disk central SB	30
4.6	Distances, K_s -band luminosity and mass-to-light ratios	33
4.7	Stellar masses	34
4.8	2MASS comparison for J0740-22	35
4.9	2MASS comparison for J0741-30A	36
4.10	2MASS comparison for J0730-28	37
B.1	HIZOA galaxies observed with the IRSF	46

Chapter 1

Introduction

1.1 Astronomy in the Zone of Avoidance

The obscuring effects of dust and star crowding at low galactic latitudes have long hampered the detection of galaxies that lie behind the disk of the Milky Way. This Zone of Avoidance (ZoA) encompasses more than 20% of the optical extragalactic sky and nearly 10% of the infrared extragalactic sky (Kraan-Korteweg & Lahav, 2000). The optical ZoA is largely due to dust extinction, which increases towards the Galactic equator where it can reach up to 70 mag in the B -band (Schlegel, Finkbeiner, & Davis, 1998). Star crowding near the Galactic bulge causes source confusion and the ZoA there increases from $|b| \lesssim 5^\circ$ to $|b| \lesssim 20^\circ$. The Zone of Avoidance in the near infrared (NIR), which is particularly sensitive to the old stars, is determined largely by stellar density. Thus, the NIR ZoA is broader near the Galactic bulge.

The Milky Way and Local Group experience a peculiar motion with respect to the Cosmic Microwave Background (CMB) (Kogut et al., 1993) due to the irregular distribution of matter in the universe. In order to understand the streaming motions of galaxies one must quantify the mass distribution. However, incompleteness in and around the ZoA, severely inhibits this process and it becomes important to map the three dimensional distribution of ZoA galaxies. NIR observations are more effective in penetrating the ZoA because the extinction due to dust is up to an order of magnitude less than in the optical. Because the NIR is less affected by bursts of star formation, it provides a better estimate of the galaxy mass which is important for determining the dynamics of the local universe.

We give here a brief description of some of the systematic surveys that have been conducted in the ZoA at different wavelengths. See Kraan-Korteweg & Lahav (2000) and Kraan-Korteweg (2005) for a comprehensive review of ZoA astronomy and the status of ZoA observations.

1.1.1 Multiwavelength Surveys

The degree and extent of the ZoA depends on the wavelength of observation. A multiwavelength approach has been most effective at detecting galaxies within the ZoA and provides complementary information from the different wavebands. A number of systematic surveys have been conducted using different parts of the electromagnetic spectrum.

Optical

Nearly two decades of deep optical studies of the ZoA have revealed tens of thousands of galaxies behind the plane of the Milky Way (see for example Kraan-Korteweg & Lahav, 2000; Wakamatsu et al., 1994). Although the optical wavelengths are most affected by dust extinction, a significant reduction of the ZoA has been achieved through systematic deep surveys covering most of the low latitudes. These surveys have been particularly effective for moderate extinction (B -band extinction, $A_B \lesssim 3$ mag) (Kraan-Korteweg, 2000) at intermediate latitudes ($|b| \gtrsim 5^\circ$). Optical surveys remain unbiased towards any specific morphological type.

Near Infrared

The longer wavelength NIR ($0.75 - 5 \mu\text{m}$) searches become more efficient where deep optical surveys become incomplete ($A_B \gtrsim 3$ mag) because extinction in the NIR is much lower than the optical: the extinction in the NIR J , H and K_s bands is approximately 45%, 21%, 14% and 9% of the B -band extinction (Schröder et al., 1997). The high resolution and sensitivity of NIR surveys makes them sensitive to both early and late-type galaxies.

There have been two major systematic surveys in the NIR: the DEep Near Infrared Southern Sky Survey (DENIS) (Epchtein et al., 1997) and the 2 Micron All Sky Survey (2MASS) (Strutskie, 2006) which imaged the whole sky in J , H and K_s . 2MASS produced a catalogue of 0.5 billion Milky Way stars and 1.65 million extended sources (galaxies) (Jarrett et al., 2000b). The 2MASS extended source catalogue (2MASX) has been used to map large scale structure in the ZoA (Jarrett, 2004; Jarrett et al., 2000a). However, galaxies near the Galactic bulge are still largely obscured due to the high stellar density and confusion.

Far Infrared

The even longer far infrared (FIR) wavelengths are hardly affected by dust extinction. The Infrared Astronomical Satellite (IRAS), working at 12, 25, 60 and $100 \mu\text{m}$ produced a Point Source Catalogue (PSC) of 250 000 sources. The low resolution of the instrument means that galaxies are not identified by their physical extent, but rather by their flux ratios in the four bands. Starburst and spiral galaxies emit strongly in the FIR and are easily detected while early type ellipticals and dwarfs are missed. However, the survey was limited at low Galactic latitudes due to the high source counts of Galactic objects and source confusion.

A follow-up redshift survey of galactic sources in the PSC (PSCz) was conducted by Saunders et al. (2000b) which allowed for three-dimensional mapping of the sources. This was later extended to the Behind the Plane (BTP) survey (Saunders et al., 2000a) which resulted in a considerable reduction of the IRAS ZoA.

Radio

The neutral hydrogen (HI) 21 cm emission line has shown to be the most effective method of penetrating the most obscured parts of the ZoA. First predicted theoretically by van der Hulst in 1944 (Karttunen et al., 2003) and subsequently detected astronomically by Ewen & Purcell (1951), the weak 21 cm or 1.42 GHz emission results from the neutral hydrogen undergoing a hyperfine transition between spin states. Despite the fact that an average hydrogen atom would take 11 million years to undergo this transition spontaneously (Landowitz & Marshall, 1960), there are enough hydrogen atoms in galaxies at low enough densities for these transitions to occur. The absorbing dust in the Milky Way is fully transparent to radiation at 21 cm, making galaxies easy to detect in the ZoA. Moreover, the emission line nature makes it possible to determine at once the redshift and rotation properties of the source. The HI content is related to morphology: elliptical galaxies have a lower HI content than spirals and dwarf irregulars. HI surveys are thus not sensitive to gas-poor elliptical galaxies.

The search for galaxies behind the Milky Way in HI was pioneered by Kerr & Henning (1987) using the Greenbank 91 m radio telescope, while the first systematic survey in the northern ZoA was the Dwingeloo Obscured Galaxies Survey (Henning et al., 1998). The introduction of the Multibeam (MB) receiver on the 64 m Parkes* telescope in 1997 brought with it the capability for more sensitive larger systematic surveys with higher survey speed (see for example Staveley-Smith et al., 1998). The MB receiver, consisting of 13 beams in a focal plane array (Staveley-Smith et al., 1996), has uncovered thousands of galaxies in two key surveys: one Southern all sky survey (HIPASS) and another deeper survey covering the ZoA (HIZOA).

HIPASS The HI Parkes All Sky Survey

The largest HI survey carried out thus far was a blind survey of the southern sky with an rms noise of 13 mJy beam⁻¹, covering a velocity range of $-1200 \lesssim cz \lesssim 12700$ km s⁻¹. A total of 5317 galaxies were found: the original survey produced a catalogue of 4315 galaxies for $\delta < +2^\circ$ (Meyer et al., 2004), while the Northern Extension ($2^\circ < \delta < +25^\circ$) produced a further 1002 galaxies (Wong et al., 2006).

HIZOA The HI Parkes Deep Zone of Avoidance Survey

This systematic survey ran with an exposure time five times longer than HIPASS, resulting in an average rms noise of 6 mJy beam⁻¹ and covering $196^\circ \leq l \leq 52^\circ$ over the same velocity range (Henning et al., 2005). The original survey ($212^\circ \leq l \leq 36^\circ$,

*The Parkes telescope is part of the Australia Telescope which is funded by the Commonwealth of Australia for operation as a National Facility managed by CSIRO

$|b| < 5^\circ$) was extended to include a northern region, the Northern Extension (NE) covering $36^\circ < l < 52^\circ$ and $196^\circ < l < 212^\circ$ with $|b| < 5^\circ$ and which yielded a further 77 galaxies (Donley et al., 2005). In addition, it has been further extended into the Galactic Bulge region (GB extension) covering $332^\circ < l < 36^\circ$, $5^\circ < |b| < 10^\circ$ and $352^\circ < l < 24^\circ$, $10^\circ < |b| < 15^\circ$ (Shafi, 2008).

1.1.2 Motivation for NIR Follow-up Studies

Follow-up near infrared observations of HI detected galaxies have been conducted with the InfraRed Survey Facility (IRSF) in Sutherland (Shafi, 2008). The IRSF telescope allows for simultaneous imaging in the three NIR pass bands: J , H and K_s . The HI data provide information on the redshift, galaxy rotation and HI mass, but no information on stellar content, in particular stellar mass. Infrared imaging can provide further information on their morphologies, inclinations and luminosities. NIR luminosities are particularly useful since the NIR mass to light ratio is nearly independent of star formation history and is more robustly predicted by theoretical models, thereby providing a cleaner estimate of the stellar mass (Bell et al., 2003).

Studying the characteristics of galaxies in the large scale structure in the ZoA, in particular in and around the Local Void, will determine any relationship between their properties and the local galaxy density.

Although many of these HI detections will have counterparts in the 2MASS Extended Source Catalogue (2MASX), we require deeper and better resolved images. The SIRIUS camera on the IRSF is ideally placed to provide this. With a pixel scale of $0''.453 \text{ pix}^{-1}$ compared to $2'' \text{ pix}^{-1}$ on 2MASS, the resolution is ~ 4.5 times better. Figure 1.1 shows the improved resolution of IRSF over 2MASS for one of the galaxies studied in this project.

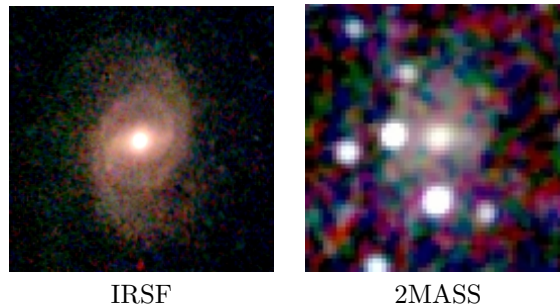


Figure 1.1: A resolution comparison between IRSF (star-subtracted) and 2MASS images for J0730-28. Both images are $1' \times 1'$. The IRSF image was taken with a ~ 10 min exposure whereas the 2MASS image had a much shorter exposure of ~ 10 s. In both images North is up and East is left.

1.2 Extinction

The interstellar medium (ISM) scatters and absorbs light, leading to a reduction of in the light received from stellar sources. This process is known as *extinction* (see for example Cardelli et al., 1989; Glass, 1999). The Zone of Avoidance flares up due to the increasing amount of dust in the Galactic plane. Extinction has a wavelength dependence; it is greater for shorter wavelengths. While the extinction in the near infrared is not negligible, it is considerably lower than at optical wavelengths. The net result is that objects will appear fainter and redder (since shorter, bluer, wavelengths are preferentially extinguished), than if there were no intervening dust. Extended objects will also appear smaller in extent, since the fainter outer parts will drop below the detection limit. To account for extinction, the distance modulus must be modified by adding the extinction at wavelength λ , A_λ , in magnitudes,

$$m - M = 5 \log D + 25 + A_\lambda \quad (1.1)$$

where m and M are the apparent and absolute magnitudes in a given band and D is the distance in megaparsecs.

1.2.1 Extinction Laws

The nature of the scattering depends on the relative sizes of the dust grains and the wavelength of light. The size of the grains also depends on the environment; denser regions have larger grains (Cardelli, Clayton, & Mathis, 1989). Since the density of the ISM varies across the sky, so will the extinction. The amount of extinction can be quantified via an extinction law parameterised by

$$R_V \equiv \frac{A_V}{E(B - V)} \quad (1.2)$$

This represents the ratio of total to selective extinction (also known as the colour excess). The parameter R_V is derived from the optical/NIR extinction and serves as an indicator of environment. The typical value of R_V for the ISM is 3.1, but it may increase up to ~ 5 in dense regions (Glass, 1999). At longer wavelengths ($\lambda > 0.9 \mu\text{m}$), the extinction is only weakly dependent on R_V , thus it will be nearly the same for all lines of sight. Cardelli, Clayton, & Mathis (1989) find an empirical extinction law

$$\left\langle \frac{A_\lambda}{A_V} \right\rangle = a(x) + \frac{b(x)}{R_V} \quad (1.3)$$

where $x \equiv 1/\lambda$. Over the wavelength range $0.9 \mu\text{m} \leq \lambda \leq 3.3 \mu\text{m}$ ($0.3 \mu\text{m}^{-1} \leq x \leq 1.1 \mu\text{m}^{-1}$) they find

$$\begin{aligned} a(x) &= 0.574x^{1.61} \\ b(x) &= -0.527x^{1.61} \end{aligned}$$

This is for the case of a single wavelength. However, for observations through a broad band filter, a correction needs to be made for the bandwidth.

1.2.2 Extinction Maps

The dust maps of Schlegel, Finkbeiner, & Davis (1998) are widely used for determining the extinction for a given line of sight. This all-sky 100 μm map combines data from the Differential InfraRed Background Explorer (DIRBE) on the COsmic Background Explorer (COBE) satellite and the InfraRed Astronomy Satellite (IRAS) Sky Survey Atlas (ISSA). Because dust emits strongly at these wavelengths, the intensity data can be transformed to a map of dust column density which is calibrated to give the reddening $E(B - V)$ for each line of sight. Extinction laws may then be used to obtain the extinction in a given waveband.

However, due to the high density and contamination by bright sources in the Galactic plane, Schlegel et al. (1998) warn that their dust maps are not calibrated and are thus poorly constrained for $|b| \lesssim 5^\circ$. In the Zone of Avoidance, both the Schlegel map and the older reddening maps of Burstein & Heiles (1982) predict reddening which is too high by $\sim 13 - 33\%$ (see for example Burstein, 2005; Dutra et al., 2002; Schröder et al., 2005).

1.2.3 Internal Extinction

Dust within other galaxies results in *internal* extinction, A^i . The amount of dust extinction is dependent on the inclination of the galaxy: a line of sight through a more inclined galaxy will have a higher dust column density and thus experience more extinction. It also depends on the morphology: while late-type irregular galaxies have a higher fractional dust content, they are also smaller and thus have less total dust and therefore lower internal extinction. This may lead to an intrinsic variation of the apparent properties of galaxies. The amount of internal extinction is often determined statistically from a very large sample and follows

$$A^i = \alpha + \beta \log(a/b)$$

In a study of near infrared extinction in spiral galaxies using 2MASS data, Masters, Giovanelli, & Haynes (2003) parameterise the internal extinction as

$$A_\lambda^i = \gamma \log(a/b) \tag{1.4}$$

where a/b is the axis ratio of the galaxy. For low inclination $\log(a/b) \leq 0.5$ they find a linear relation with

$$\begin{aligned} \gamma_J &= 0.48 \pm 0.15 \\ \gamma_H &= 0.39 \pm 0.15 \\ \gamma_{K_s} &= 0.26 \pm 0.15 \end{aligned}$$

For high inclinations, $\log(a/b) > 0.5$, they find

$$\begin{aligned}\gamma_J &= (1.6 \pm 0.2) + 0.24/\log(a/b) \\ \gamma_H &= (1.4 \pm 0.2) + 0.20/\log(a/b) \\ \gamma_{K_s} &= (1.1 \pm 0.2) + 0.13/\log(a/b)\end{aligned}$$

1.3 Spectrophotometric Galaxy Modelling

Evolutionary population synthesis has become a standard technique to study the spectrophotometric evolution of galaxies since its inception in the early 1970's (see for example Tinsley, 1980; Bruzual, 1983). Computational models can be used to determine the spectral flux of a galaxy over a wide range of wavelengths, or the Spectral Energy Distribution (SED). These models take into account the evolutionary history of the galaxy and use a library of Single Stellar Populations (SSP) to synthesise the galaxy spectrum, which in the simple case is the sum of all the spectra of the individual stars. The quality of a given population synthesis model therefore relies primarily on the quality and completeness of the stellar data (Charlot & Bruzual, 1991). Over the past two decades, improved observations and models of stars, particularly of Asymptotic Giant Branch (AGB) stars, have significantly improved the stellar libraries.

The spectrophotometric models of hypothetical dust-free galaxies should be independent of geometry and inclination, however, the presence of dust introduces a strong dependence on the distribution of stars and interstellar material and vastly complicates the determination of the SED. Dust is a very important part of the interstellar medium (ISM) and plays an important role in transferring radiation from stellar sources. It absorbs and scatters photons with wavelengths shorter than about $1 \mu\text{m}$ (optical, UV); absorbed photons are re-radiated in the infrared. As a result, the SED of a galaxy can be substantially altered, particularly in galaxies undergoing massive amounts of starformation (Silva et al., 1998). Nevertheless, many early papers neglected the radiative processes in the dusty interstellar medium (Bruzual & Charlot, 1993), while some later papers include it only partially or over simplified.

1.3.1 GRASIL code

In this project we use the GRASIL models of Silva et al. (1998); these model the photometric evolution of galaxies with particular emphasis on the dusty interstellar medium, from ultraviolet to submillimeter wavelengths. They take into account three different dusty environments:

1. dust in interstellar neutral hydrogen (HI) clouds heated by the interstellar radiation field, the “cirrus” component;
2. dust associated with starforming molecular clouds and ionised hydrogen (HII);
3. dust within circumstellar shells produced in the windy final stages of stellar evolution.

The different environments clearly have varying importance in different galactic systems and at different stages of galactic evolution. The GRASIL code aims to simulate any Hubble type at all evolutionary stages. An example of three of the GRASIL models is given in Figure 1.2. All the models have very similar near infrared emission, the region of interest in this project; the NIR emission is largely due to the old stellar population and is little affected by dust. The morphology independent nature of the SEDs in the NIR is reflected in the morphology independence of galaxy NIR colours.

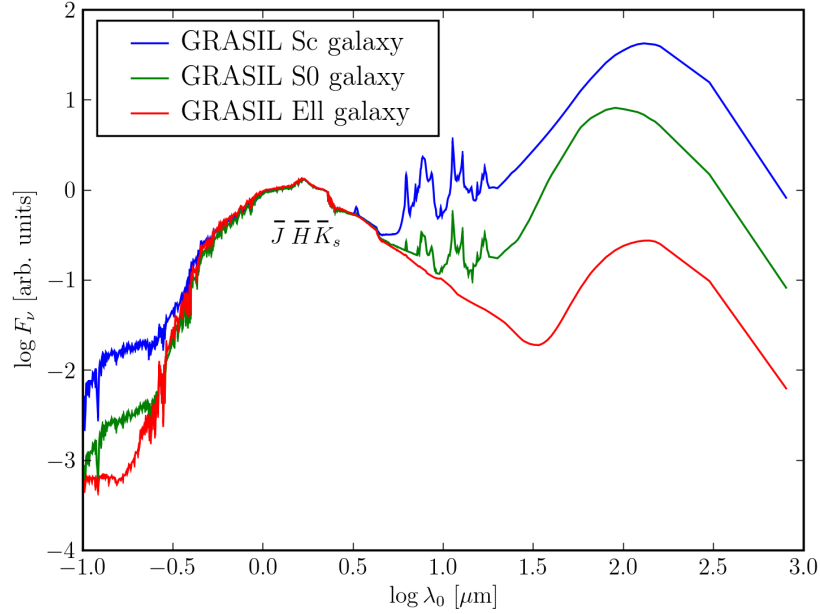


Figure 1.2: GRASIL SEDs for Sc, S0 and Elliptical galaxies. The positions of the three NIR bands, J , H and K_s , are indicated.

1.3.2 SED extinction fitting

We use the SED models, not as an indication of evolutionary history, but as an indication of the expected SEDs of galaxies. Photometry of our galaxies will provide apparent magnitudes that are fainter than expected due to dust extinction. Since the dust extinction follows the extinction law, it can be parameterised with a single value, the visual extinction, A_V . By taking this into account we can fit our fluxes (converted from magnitudes) to the model or expected spectral energy distribution, thereby obtaining the “best fit” extinction value.

1.4 Outline

In this project we undertake near infrared photometric studies of four galaxies detected in an HI survey of the Zone of Avoidance. We aim to determine the photometric properties of the galaxies. The HI data provides information on redshift (indirectly distance), rotation

and HI mass, whereas NIR imaging can provide information on morphology, inclination and most importantly, the stellar mass.

In Chapter 2 we provide details of the near infrared observations and the initial data reduction with IRAF. Chapter 3 gives the data analysis: we describe the photometric corrections for extinction and redshift as well as the method of spectral energy distribution fitting used for determining the extinction. In Chapter 4 we discuss the results, including the disk scale lengths and stellar masses. The final Chapter 5 provides a summary of results and a discussion of possible future work.

Chapter 2

Observations and Data Reduction

2.1 Near Infrared Observations

Imaging in the near infrared part of the spectrum makes use of two-dimensional array detectors which count photons. These detectors are similar in design to the charge coupled devices (CCDs) in optical astronomy. Both employ the same physical principles for detecting photons and converting their energy to an electronic signal. A photon striking a semiconductor material may impart enough energy to release an electron, provided the energy of the photon exceeds the bandgap energy of the semiconductor. This *photoelectric effect* is the underlying physical mechanism whereby photons are converted to electrons which can subsequently be measured electronically.

Originally developed for the NICMOS instrument on the Hubble Space Telescope, the HgCdTe (mercury cadmium telluride) array detectors are now widely used for NIR astronomy. The two-layer detector consists of HgCdTe on a sapphire substrate which forms the detector and a silicone-based multiplexer which handles the electric charge (Glass, 1999). The multiplexer allows the charge to be read out pixel by pixel. Because of the relatively low energy of NIR photons, the construction of these arrays is difficult and they are imperfect, often suffering from defects.

Furthermore, NIR observations are adversely affected by the high thermal noise and atmospheric effects which result in a very high background noise. Since the radiation from objects with temperatures of a few hundred Kelvin (room temperature) peaks in the NIR, the surroundings (everything in or near the telescope) will radiate at wavelengths in the NIR. Although this can be reduced by the cooling of the instruments, detectors and the telescope itself, the effect cannot be nullified and the thermal background remains high. As a result NIR astronomers employ various techniques to overcome these particular problems.

2.1.1 Dithering

One of the major problems with IR detectors is the large numbers of *bad pixels*; a bad pixel is an imperfect or malfunctioning pixel in the detector array. In addition to dead pixels the sensitivity or response to light varies from pixel-to-pixel across the array. The problem of dead pixels can be overcome by employing a method known as *dithering*. A sequence of short exposures is taken, in which the pointing of the telescope is offset along a circle centred on the target coordinates; the radius of this circle is called the dither radius (typically a few arcseconds). In this way light from the target will fall on different pixels in each exposure. A single image may be produced by realigning the individual exposures and combining them. The effects of the bad pixels can be removed by using a median-combine as opposed to simple averaging.

2.1.2 Flat-fielding and Dark Subtraction

Pixel-to-pixel variations in sensitivity are corrected for by *flat-fielding*. If an exposure is taken of a uniformly illuminated source, the variations in the resulting image will directly represent the response of each pixel to photons. The twilight sky usually provides a good source of uniform light over the typical field of view of a telescope. Alternately, a white screen in the telescope dome illuminated by an incandescent light may be imaged. Many such individual *flat* images are usually combined to produce a low noise master flat, thereby allowing the pixel-to-pixel variations in sensitivity to be removed from an image by dividing by this master flat.

The relative low energy of NIR photons means that the detectors are particularly susceptible to thermal electrons originating from the telescope environment. These electrons can cause charge to build up in the detector even while the shutter is closed. A *dark* image is obtained by exposing the array with the shutter closed for the same time as the object exposures. Since this dark current is always present, all images must have the dark image subtracted from them.

2.1.3 Sky Subtraction

The NIR sky is particularly bright, much brighter than the optical sky. Light is scattered off dust, air molecules and aerosols, and absorbed by water and carbon dioxide molecules in the atmosphere. In general, NIR observations are hampered by the high background and frequent saturation due to emission from the atmosphere and surroundings. For wavelengths longer than $\sim 2 \mu\text{m}$ the emission is mostly due to scattered moonlight, starlight and atmospheric hydroxyl (OH) emission (Glass, 1999). Moreover, the atmospheric emission is not constant in time, with variations on timescales of a few minutes, nor is it constant in space, with significant gradients across a single image (typically a few arcminutes). Saturation can be avoided by reading the array out more frequently, i.e. making and combining many short exposures, while the sky variations can be reduced by accurate subtraction and monitoring on short timescales.

Sky fields can be obtained by median-combining the object images without first aligning them in a process known as *self-sky*. In this way one obtains a field essentially free of sources, provided that the dither radius is larger than any extended sources in the image. Alternatively, a separate exposure can be taken of a nearby patch of sky. The sky image is subtracted from the object image.

2.2 Target Selection

Our galaxies are selected from the list of all HI galaxies detected in the HI Parkes deep Zone of Avoidance survey, HIZOA (for an overview of ZoA observations see §1.1). The original survey and the two extensions were done using the 21 cm multibeam receiver on the Parkes 64 m radio telescope. The receiver consists of 13 beams, each with two orthogonal linear polarisations, and an average beamwidth of $14'.3$. The correlator has a bandwidth of 64 MHz, with 1024 channels having a spacing of 13.2 km s^{-1} . The velocity coverage is $-1,200 \text{ km.s}^{-1} < cz < 12,700 \text{ km s}^{-1}$ and the average system temperature is 20 K (Donley et al., 2005). With an average integration time of 20 min/beam and after Hanning smoothing, the rms noise per beam is 6.0 mJy. The resulting velocity resolution is 27 km s^{-1} . The three-dimensional (two spatial and one velocity) data cubes were searched by eye for detections where three independent searchers examined each of the three possible planes (right ascension-declination, right ascension-velocity and declination-velocity) for possible sources. Finally, a fourth person cross-checked and compiled the final galaxy list. Our sample is thus obviously biased towards spiral galaxies having a large HI content.

The observations in this report form part of an on-going NIR follow-up study of the galaxies found in the HIZOA survey. A number of people in the Astronomy Department at UCT have contributed to the observations.

2.3 IRSF Observations

The IRSF data used in this project were obtained by Nebiha Shafi in April 2007 using the Japanese InfraRed Survey Facility (IRSF) at the South African Astronomical Observatory (SAAO) site in Sutherland. The IRSF is a 1.4 m alt-azimuthal Cassegrain telescope equipped with a detector capable of simultaneously imaging in the 3 NIR bands J ($\lambda_c = 1.25 \mu\text{m}$), H ($1.63 \mu\text{m}$) and K_s ($2.14 \mu\text{m}$). The Simultaneous three-colour InfraRed Imager for Unbiased Survey (SIRIUS) camera consists of three $1024 \text{ pixel} \times 1024 \text{ pixel}$ HgCdTe (HAWAII) arrays (Nagashima et al., 1999; Nagayama et al., 2003). It has a $7'.7 \times 7'.7$ field of view and a pixel scale of $0''.453 \text{ pixel}^{-1}$.

SIRIUS has broad band J , H and K_s filters which are similar to the filters used in the 2 Micron All Sky Survey (2MASS). 2MASS had a slightly smaller aperture of 1.3 m with a $8'.5 \times 8'.5$ field of view and a pixel scale of $2'' \text{ pixel}^{-1}$ (Strutskie, 2006). The different pixel scales results in a ~ 4.5 times improvement in resolution of IRSF/SIRIUS over 2MASS. Furthermore, IRSF's faster focal ratio of $f/10$ (2MASS, $f/13.5$) means that it can go deeper

or reach greater sensitivity with shorter exposures. The exposure times for 2MASS are typically 6×1.3 s, while for IRSF we have used 25×24 s exposures. The smaller pixel scale, longer exposures and faster speed makes IRSF/SIRIUS ideal for these type of follow-up observations.

Each image is made from 25×24 s dithered exposures, yielding a total integration time of 600 s. The dithering radius was $15''$. We selected only galaxies observed under good seeing, denoted by a “1” in the observation logs. A list of the galaxies with their coordinates and HI parameters is given in Table 2.1. The HI spectra for the galaxies may be found in Appendix A.

Name	RA [hh mm ss]	dec [° ' '']	l [deg]	b [deg]	V [km.s ⁻¹]	M_{HI} [$10^9 \mathcal{M}_{\odot}$]
J0740-22	07 40 58	-22 54 42	238.816	-0.098	3051	3.47
J0741-30A	07 41 43	-30 29 37	245.496	-3.698	7502	20.4
J0731-27	07 31 23	-27 19 24	241.618	-4.141	7302	11.9
J0730-28	07 30 45	-28 23 52	242.500	-4.773	8093	29.6

Table 2.1: List of galaxies and their coordinates, velocities and HI masses from the HI data.

2.4 Data Reduction

2.4.1 SIRIUS Pipeline

The initial data reduction was done by P. A. Woudt, following the standard NIR array image reduction procedure. This involved the dark subtraction, flat-fielding, sky-subtraction and dithered image combination as discussed in §2.1. To implement this we use the dedicated SIRIUS* pipeline, loaded as a package in the standard image reduction suite IRAF[†]. The pipeline is used to

1. subtract the dark image;
2. divide by flat-field image (usually constructed from twilight flats);
3. subtract sky image (either self-sky or nearby image); and
4. align and median-combine dithered frames.

Further IRAF routines were used to subtract stars from the images (`killall`) and perform an astrometric calibration on the K_s -band image (`ccmap`) to which the other images are aligned.

2.4.2 Images

The star-subtracted images of the four galaxies are given in Figure 2.1.

*<http://optik2.mtk.nao.ac.jp/%7Eyas/pipeline/manual/pipeline020510-e.html>

[†]Image Reduction and Analysis Facility - IRAF is distributed by the National Optical Astronomy Observatories, which are operated by the Association of Universities for Research in Astronomy, Inc., under cooperative agreement with the National Science Foundation.

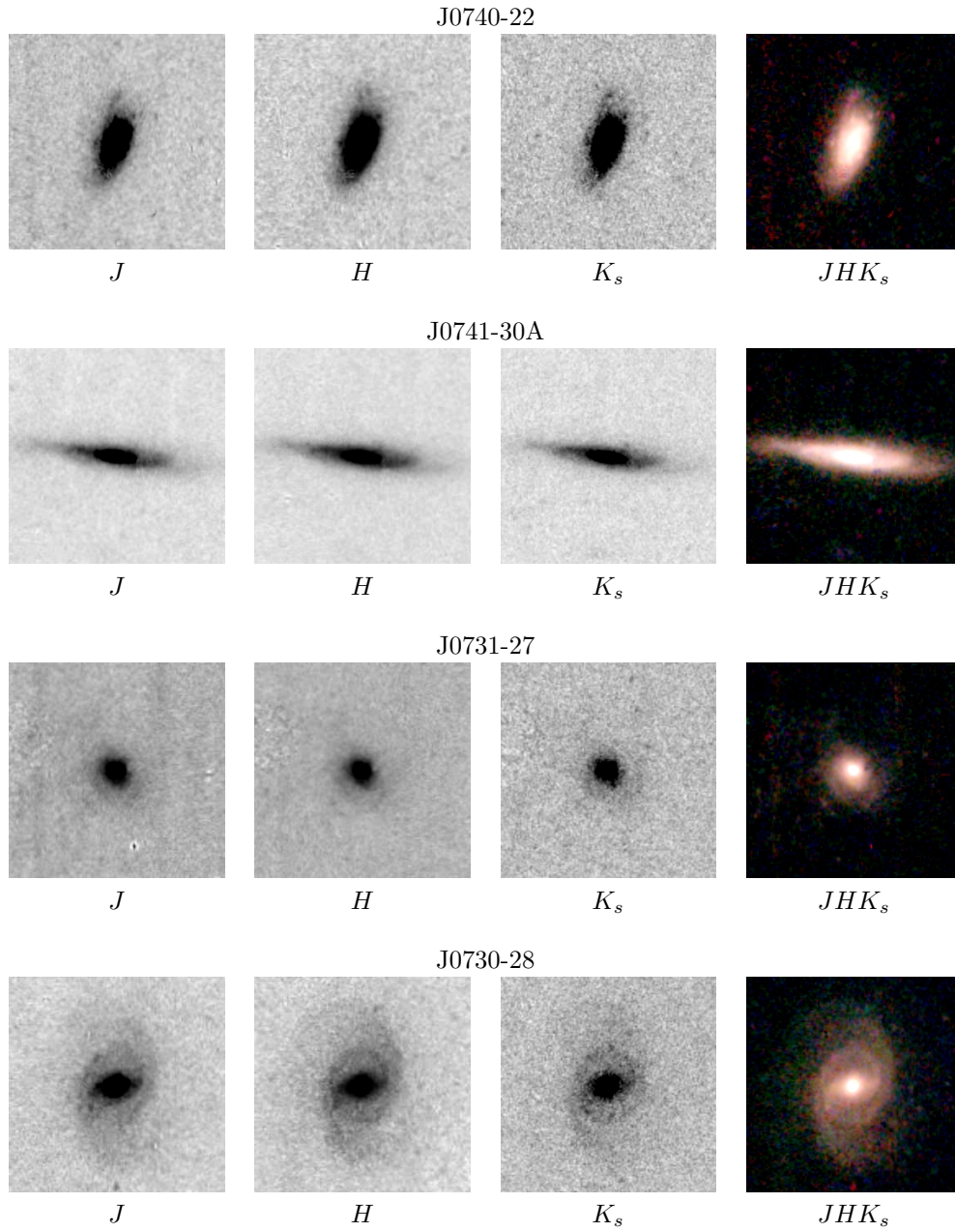


Figure 2.1: Star-subtracted J , H , K_s and three-colour JHK_s images of the galaxies. The stamps are all $1' \times 1'$ with North at the top and East on the left.

2.4.3 Magnitude Zero-Points

It is necessary to first to convert the instrumental counts to calibrated magnitudes and then to convert the calibrated IRSF/SIRIUS magnitudes into a standard system to facilitate direct comparison. This is done with magnitude zero points (ZPs) and transformation equations. The 2MASS system is an excellent standard: it is widely used, its Point Source Catalogue (2MASS-PSC) covers most of the sky, the calibration is smooth over the whole sky and transformation equations to other major systems already exist. The IRSF/SIRIUS filters, while very similar to the 2MASS filters, are different enough that we cannot directly obtain magnitudes in the 2MASS system. Nakajima et al. (2008) derive transformation equations to convert colours and magnitudes measured by IRSF/SIRIUS into the 2MASS system:

$$\begin{aligned} J_{2\text{mass}} &= J_{\text{sirius}} + (0.049 \pm 0.009)(J - H)_{\text{sirius}} \\ H_{2\text{mass}} &= H_{\text{sirius}} + (-0.029 \pm 0.008)(J - H)_{\text{sirius}} \\ K_{s,2\text{mass}} &= K_{s,\text{sirius}} + (-0.016 \pm 0.006)(J - K_s)_{\text{sirius}} \end{aligned} \quad (2.1)$$

These are valid over wide colour ranges $0.0 \leq (J - H) \leq 3.9$, $0.0 \leq (H - K_s) \leq 2.8$ and $0.0 \leq (J - K_s) \leq 4.9$.

The magnitude zero point offsets provide the calibration between counts and magnitudes. 2MASS stars in the object frames are used to calibrate the photometry. Stars in the field are matched to a catalogue of 2MASS stars near the object. The 2MASS magnitudes of these stars are transformed into the IRSF/SIRIUS system using the inverse forms of equations 2.1 (Nakajima et al., 2008). An *instrumental magnitude*, m_{instr} ,

$$m_{\text{instr}} = -2.5 \log \left(\frac{\text{counts}}{s} \right) \quad (2.2)$$

is then obtained for each of these stars. The zero point offset is the difference between the instrumental magnitude and the catalogue magnitude, m_{sirius} ,

$$\text{ZP} \equiv m_{\text{sirius}} - m_{\text{instr}} \quad (2.3)$$

We obtain a ZP for each star in the image; averaging yields a single ZP offset for that frame. The ZP can then be used to obtain the IRSF/SIRIUS magnitude for any source within that frame. For comparison we can convert back to the 2MASS system via equations 2.1.

2.4.4 Photometry

The following procedure, utilising tasks in IRAF packages, was used to obtain the Surface Brightness Profiles (SBPs) and magnitudes of all four galaxies in the three NIR bands. Initially, the magnitude is obtained by fitting an elliptical aperture to each galaxy; a single elliptical aperture was used for each band.

Central Coordinates and Sky Values

The task `findgalcoor` was used to determine the central pixel coordinates of each object and the task `radprofil` was used to determine the sky value in counts.

Ellipse Fitting

Ellipses were fitted using the task `ellipse`. We fix the central coordinates to those obtained from `findgalcoor` and allow the position angle (ϕ) and ellipticity ($\epsilon = 1 - b/a$; where a and b are the semi-major and -minor axes of the ellipse) to vary, fitting ellipses parameterised by these values at each semi-major axis. `ellipse` returns a table containing, amongst others, the intensity in counts enclosed within the ellipse, the position angle, the ellipticity and their errors at each semi-major axis step. Plotting ϵ and ϕ versus a allows us to determine the shape of the galaxy. A single value for each parameter, characteristic of the galaxy can be obtained by averaging the results from the outer parts of each galaxy since both the ellipticity and the position angle usually stabilise in the outer disk. This was done for each band and the results compared to ensure consistency. The ellipse defined by the averaged parameters and a yet to be determined radius is used as the aperture for photometry. However, since each band yields a slightly different result, we choose to use the J -band aperture for the final analysis of all three NIR bands. A list of the apertures is given in Table 2.2.

Name	X_0 [pix]	Y_0 [pix]	ϵ	ϕ [deg]
J0740-22	592.12	350.25	0.500 ± 0.023	-18.2 ± 2.5
J0741-30A	444.81	617.16	0.786 ± 0.008	82.9 ± 0.6
J0731-27	479.10	195.25	0.178 ± 0.027	37.0 ± 6.6
J0730-28	582.77	445.54	0.370 ± 0.050	2.0 ± 5.0

Table 2.2: Details of the elliptical apertures obtained from fitted J band ellipses to be used for the photometry. X_0 and Y_0 are the central pixel coordinates, ϵ the ellipticity and ϕ the position angle.

Surface Brightness Profiles and Magnitudes

We use the IRAF package `radprofil` to determine the Surface Brightness Profiles (SBPs) in each band using the above ellipses. Examining the SBPs we determine an outer radius r_{out} where the sky is reached, i.e. where the errors in the surface brightness begin to dominate. The SBPs are plotted in Figures 2.2 to 2.5 where a vertical line shows the outer radius, r_{out} , of the galaxy and horizontal lines indicate the surface brightness in each band at this radius.

The magnitude enclosed within r_{out} , m_r , is calculated from the table output of `ellipse`; an extrapolated total magnitude, m_T is also returned by `radprofil`. These results for m_r and m_T are given in Table 2.4. All magnitudes are given in the IRSF system unless otherwise stated. We note that the difference between aperture and total magnitudes is

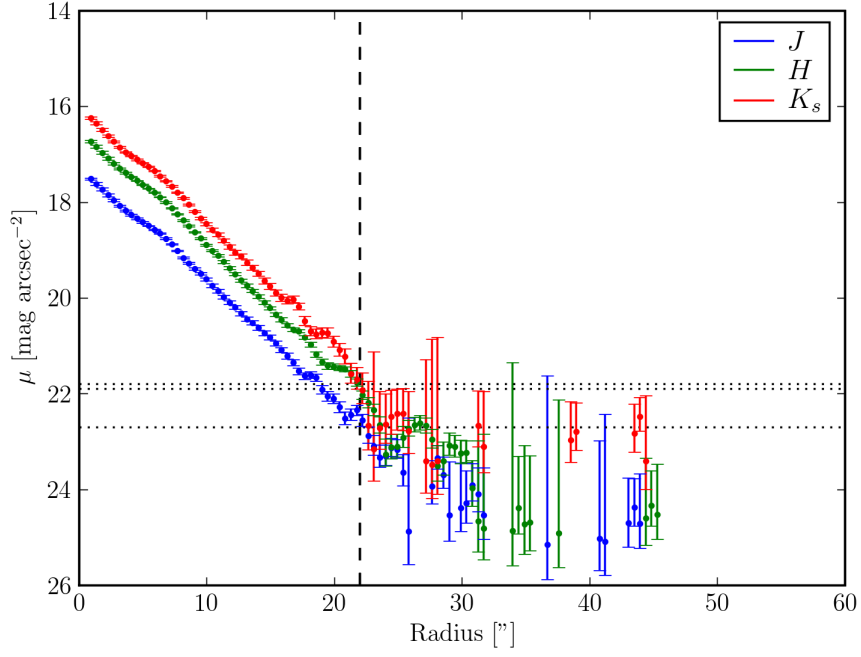


Figure 2.2: Surface brightness profiles in each band for J0740-22.

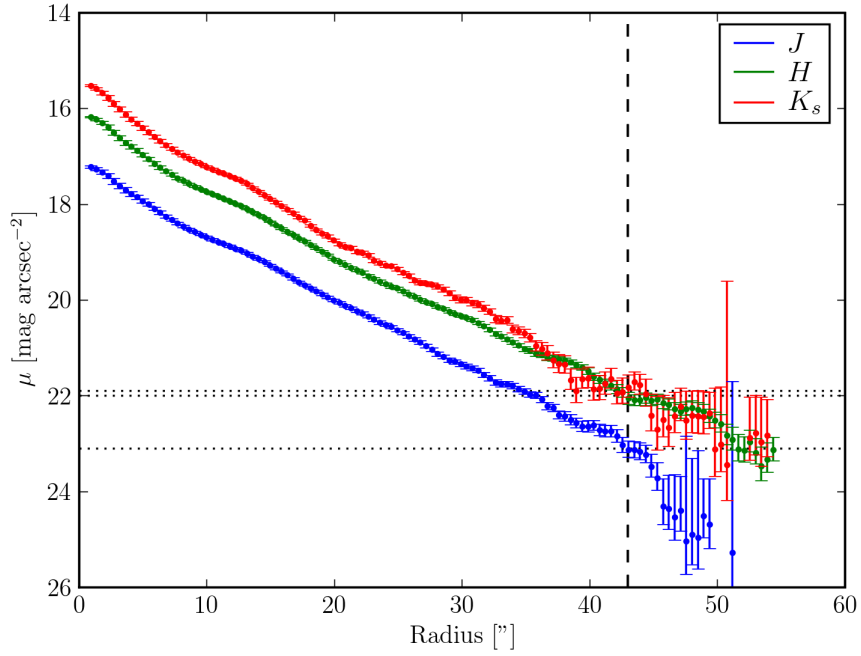


Figure 2.3: Surface brightness profiles in each band for J0741-30A.

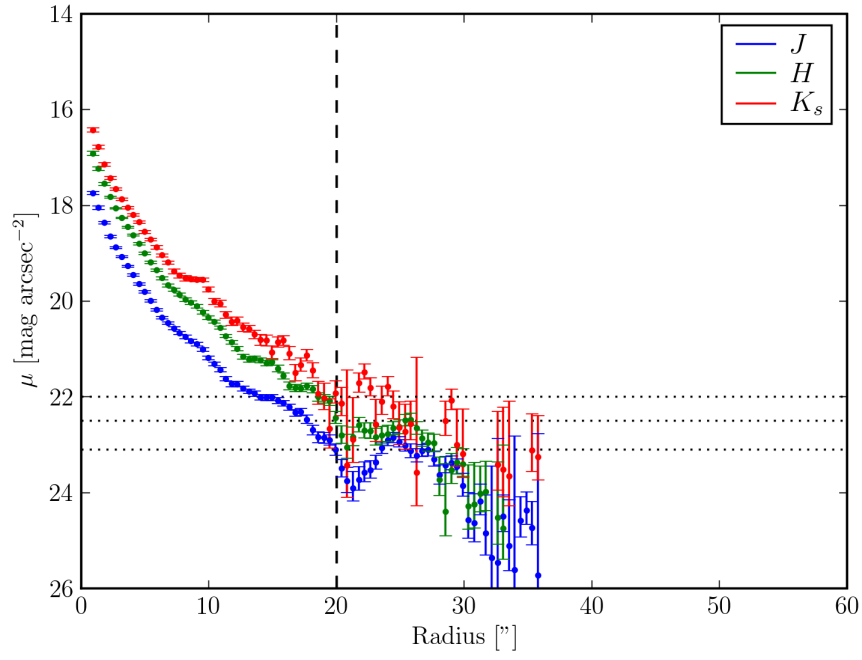


Figure 2.4: Surface brightness profiles in each band for J0731-27.

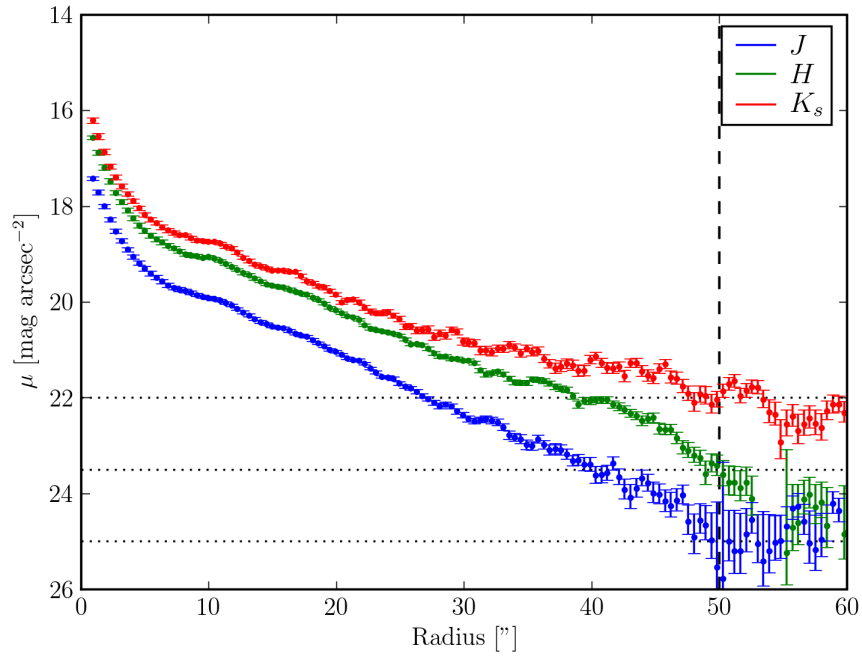


Figure 2.5: Surface brightness profiles in each band for J0730-28.

typically $0.1 - 0.2$ mag, suggesting that our apertures enclose $85 - 90\%$ of the total galaxy light.

The error in the magnitude is a result of both the zero-point errors and the sky noise. The zero point error has been determined with the zero point, whereas an estimate has to be made of the sky error. To do this we vary the sky level in **radprofil** by the intensity error at r_{out} ; the resulting change in the total magnitude calculated by **radprofil** is used as the sky-error estimate in magnitudes. Finally the total error in m_r is then $\sigma_{m_r}^2 = \sigma_{\text{ZP}}^2 + \sigma_{\text{sky}}^2$, where σ_{ZP} is the zero-point error and σ_{sky} is the sky-error.

Name	r [$''$]	μ_r [mag arcsec $^{-2}$]		
		J	H	K_s
J0740-22	23	22.7 ± 0.1	21.9 ± 0.1	21.8 ± 0.2
J0741-30A	43	23.1 ± 0.1	22.0 ± 0.1	21.9 ± 0.2
J0731-27	20	23.1 ± 0.1	22.5 ± 0.1	22.0 ± 0.2
J0730-28	50	25.0 ± 0.3	23.5 ± 0.2	22.0 ± 0.2

Table 2.3: Photometry results showing the radius, r , and the surface brightness μ_r at r for each band.

Name	r [$''$]	m_r [mag]		
		J	H	K_s
J0740-22	23	12.78 ± 0.05	12.04 ± 0.02	11.58 ± 0.07
J0741-30A	43	12.48 ± 0.06	11.56 ± 0.04	11.08 ± 0.07
J0731-27	20	13.49 ± 0.05	12.70 ± 0.05	12.24 ± 0.09
J0730-28	50	12.41 ± 0.07	11.48 ± 0.04	11.05 ± 0.09

Name	r [$''$]	m_T [mag]		
		J	H	K_s
J0740-22	23	12.74 ± 0.05	12.00 ± 0.02	11.56 ± 0.07
J0741-30A	43	12.52 ± 0.06	11.49 ± 0.04	11.08 ± 0.07
J0731-27	20	13.32 ± 0.05	12.58 ± 0.05	12.13 ± 0.09
J0730-28	50	12.28 ± 0.07	11.44 ± 0.04	10.90 ± 0.09

Table 2.4: Photometry results showing the radius, r , and the magnitudes m_r contained in that radius for each band. The total magnitudes obtained from **radprofil** are also given.

Chapter 3

Data Analysis

3.1 Photometric Corrections

The magnitudes we have derived in §2.4.4 are apparent magnitudes and are subject to extinction and cosmological effects. These effects, due to dust and the cosmological expansion, enter into the distance modulus as correction terms in a given band

$$m - M = 5 \log D + 25 + k(z) + A_{\lambda}^{g,i} \quad (3.1)$$

where D is the distance to the galaxy in Megaparsecs, $k(z)$ the cosmological k -correction due to redshift effects and $A_{\lambda}^{g,i}$ is the *total* extinction in a given direction and accounts both for Galactic extinction and internal extinction. After correcting for extinction and redshift effects, the corrected magnitude m^o satisfies

$$m^o - M = 5 \log D + 25 \quad (3.2)$$

where

$$m^o = m - k(z) - A_{\lambda}^{g,i} \quad (3.3)$$

These two corrections are explained in more detail in the following two subsections.

3.1.1 k -correction

The expansion of the universe implies that galaxies, or bound entities like groups and clusters, are perceived to move away from each other. This apparent recession motion of galaxies results in a shift of their spectral lines towards longer wavelengths which is quantified by the *redshift*, z :

$$z = \frac{\lambda - \lambda_0}{\lambda_0} = \frac{\Delta\lambda}{\lambda_0} \quad (3.4)$$

where λ_0 is the rest wavelength and λ , the observed wavelength. For small values ($\lesssim 0.1$), the redshift satisfies $z \approx v/c$, where v is the heliocentric line-of-sight recessional velocity and

$c = 2.998 \times 10^5 \text{ km s}^{-1}$ is the speed of light.

This cosmological redshift implies that light received in a given passband centred on λ was actually emitted from a *narrower* passband centred on $\lambda_0 = \lambda/(1+z)$; for broadband photometry the k -correction provides the transformation between the observed frame and the rest frame, correcting for both the change in the width of the passband and for the shift in central wavelength (Humason, Mayall, & Sandage, 1956; Oke & Sandage, 1968). The correction may be expressed as a magnitude (equations 3.1 and 3.3), consistent with the definition of Hogg et al. (2002). Note that Glass (1999) defines the k -correction with a negative sign, to be added not subtracted in equation 3.3.

The k -correction in a filter i can be calculated as follows:

$$k_i = +2.5 \log(1+z) + 2.5 \log \left[\frac{\int_0^\infty f_\lambda(\lambda) S_i(\lambda) d\lambda}{\int_0^\infty f_\lambda\left(\frac{\lambda}{1+z}\right) S_i(\lambda) d\lambda} \right] \quad (3.5)$$

where z is the redshift of the source, $f(\lambda)$ is the source spectral flux density and $S(\lambda)$ the filter bandpass function (Oke & Sandage, 1968; Poggianti, 1997). The first term accounts for the narrowing of the passband from the rest frame by a factor $(1+z)$ while the second term accounts for the shift of the spectrum within the passband. In practice this is difficult to do as it requires accurate knowledge of the source flux density, as well as the bandpass functions. The k -corrections may be found empirically by using either a model Spectral Energy Distribution or a representative one (averaged over a number of objects of the same type) as the source flux density. With knowledge of the filter response curves, the SED can be artificially redshifted to produce the k -corrections.

Glass (1999) finds that for small redshifts ($z \leq 0.2$), the k -corrections are linear in z . He gives the values for the three infrared passbands, J , H and K_s , as

$J - H$	$-0.5z$
$H - K_s$	$-3.5z$
K_s	$3.3z$

Noting again the sign inconsistency, we adopt the following k -corrections for the three near infrared bands

$$\begin{aligned} k_J &= +0.7z \\ k_H &= +0.2z \\ k_{K_s} &= -3.3z \end{aligned} \quad (3.6)$$

3.1.2 Extinction Correction

The total extinction $A_\lambda^{g,i}$ comprises $A_\lambda^g(l, b)$, the galactic (foreground) extinction and A^i , the internal extinction within the galaxy; the Galactic extinction depends on the Galactic longitude and latitude, l and b , while the internal extinction depends on the inclination, i , and morphology of the galaxy. As shown in §1.2, for a given extinction law, the total

extinction may be characterised by a single parameter: the total extinction in the V -band, A_V . Since the extinction law is usually given as a function of wavelength, to obtain the total extinction in a broadband filter, the extinction law must be integrated over the filter response function. The extinction in each IRSF/SIRIUS band is obtained by integrating the extinction law of Cardelli, Clayton, & Mathis (1989) over each of the J , H and K_s bandpasses (Cluver et al., 2008):

$$\begin{aligned} A_J &= 0.282A_V \\ A_H &= 0.177A_V \\ A_{K_s} &= 0.114A_V \end{aligned} \tag{3.7}$$

The SED fitting technique we employ here, fits the total extinction in the V -band, A_V . Thereafter we estimate the component due to internal extinction.

3.2 Spectral Energy Distributions

3.2.1 Extinction Fitting

By considering the Spectral Energy Distributions of our galaxies we find the value for the extinction which best reproduces a model SED. This determines the total extinction, both Galactic and internal. A description of spectrophotometric galaxy modelling is given in §1.3, from which we see that the spectral flux density of galaxies is nearly independent of morphology in the near infrared. This part of the spectrum is dominated by the old, red stellar population (population II) and is little affected by dust and gas. Nevertheless we choose to use the late “Sc” type model galaxy for fitting the extinction as the HI survey is most likely dominated by gas-rich spirals; we use the GRASIL models of Silva et al. (1998).

The templates are in the form of flux density versus wavelength, so we convert our 2MASS magnitudes, m , to flux density, F_ν , using the relation

$$m = -2.5 \log \frac{F_\nu}{F_{\nu,0}} \tag{3.8}$$

where F_ν is the flux density and $F_{\nu,0}$ is the flux density zero point. The flux density zero points are derived from the absolute spectral irradiance calibration in the three 2MASS NIR bands by Cohen, Wheaton, & Megeath (2003)*

$$\begin{aligned} F_{J,0} &= 1594 \text{ Jy} \\ F_{H,0} &= 1024 \text{ Jy} \\ F_{K_s,0} &= 666.7 \text{ Jy} \end{aligned} \tag{3.9}$$

where 1 Jansky (Jy) = $10^{-26} \text{ W m}^2 \text{ Hz}^{-1}$. The spectral flux density is defined as the energy

*<http://www.ipac.caltech.edu/2mass/releases/second/doc/sec4.5.htm>

per unit time per unit area per unit frequency and is a more natural unit than magnitudes when working with spectra.

Furthermore, the model SED is in arbitrary units so we need to normalise it to the source. Since the longer wavelength K_s band is least affected by extinction and traces the old stellar population, thus the galaxy itself, best, we normalise the SED template to the source K_s band flux density. The source SED differs from the template because of extinction and redshift effects: the k -correction is known a priori from the redshift and the extinction is known up to a single parameter, $A_V^{g,i}$. Thus the deviation of the source SED from the template is determined by a single parameter and it becomes simple to determine the best value of $A_V^{g,i}$ that fits the source SED to the template. By varying the amount of visual extinction, the value of $A_V^{g,i}$ for which the J and H band flux densities deviate the least from the normalised SED template, can be identified as the best fit extinction value. The error is determined by varying the extinction value until the template no longer lies within the error bars.

The extinction values thus obtained are given in Table 3.1 along with the Schlegel values for comparison; the discrepancy between the fitted values and the Schlegel values is due to internal extinction which will be discussed in §4.1. The fitted SEDs for each galaxy are shown in Figures 3.1 to 3.4 where the horizontal error bars are an indication of the bandwidth of each filter while the vertical errors are the propagated magnitude errors.

Name	$A_J^{g,i}$ [mag]	$A_H^{g,i}$ [mag]	$A_{K_s}^{g,i}$ [mag]	$A_V^{g,i}$ (fit) [mag]	A_V^g (Schlegel) [mag]
J0740-22	0.46 ± 0.03	0.30 ± 0.02	0.19 ± 0.01	1.7 ± 0.1	2.032
J0741-30A	0.60 ± 0.08	0.39 ± 0.05	0.25 ± 0.04	2.2 ± 0.3	1.381
J0731-27	0.38 ± 0.05	0.25 ± 0.04	0.16 ± 0.02	1.4 ± 0.2	2.716
J0730-28	0.46 ± 0.03	0.28 ± 0.02	0.18 ± 0.01	1.6 ± 0.1	1.784

Table 3.1: Results from fitting source SED with total visual extinction, $A_V^{g,i}$, to template SED. The extinction in each band is given as well as the Galactic extinction values of Schlegel, Finkbeiner, & Davis (1998), A_V^g , at the coordinates each galaxy for comparison.

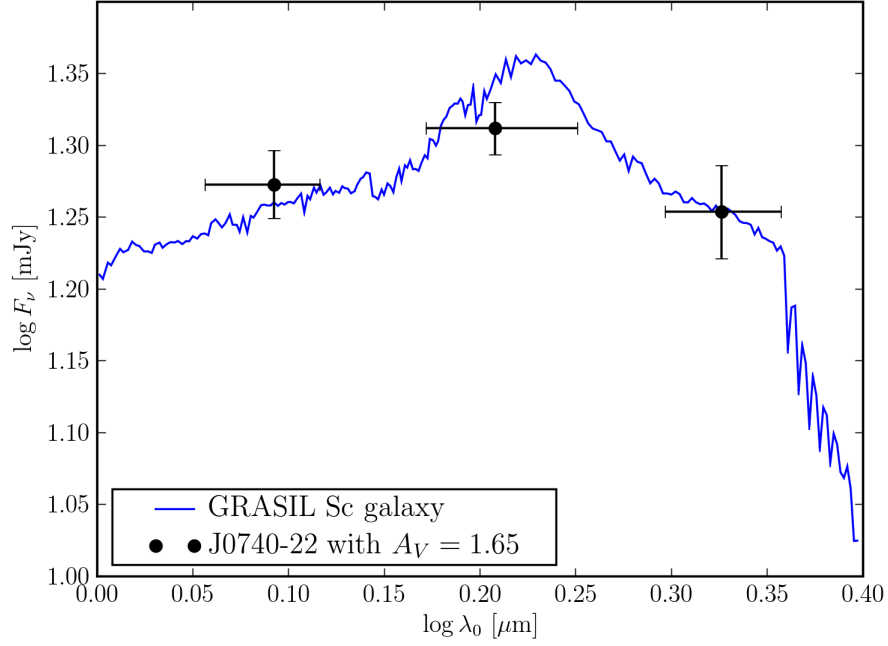


Figure 3.1: Near Infrared Spectral Energy Distribution for J0740-22, showing the extinction- and redshift-corrected flux densities in the J , H and K_s bands as well as the GRASIL template for a late-type spiral.

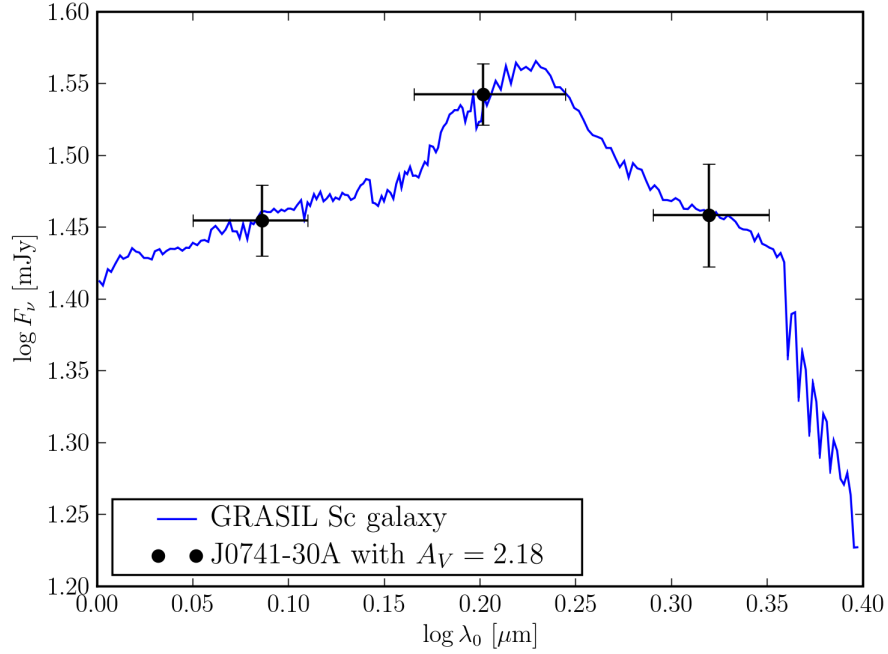


Figure 3.2: Near Infrared Spectral Energy Distribution for J0741-30A, showing the extinction- and redshift-corrected flux densities in the J , H and K_s bands as well as the GRASIL template for a late-type spiral.

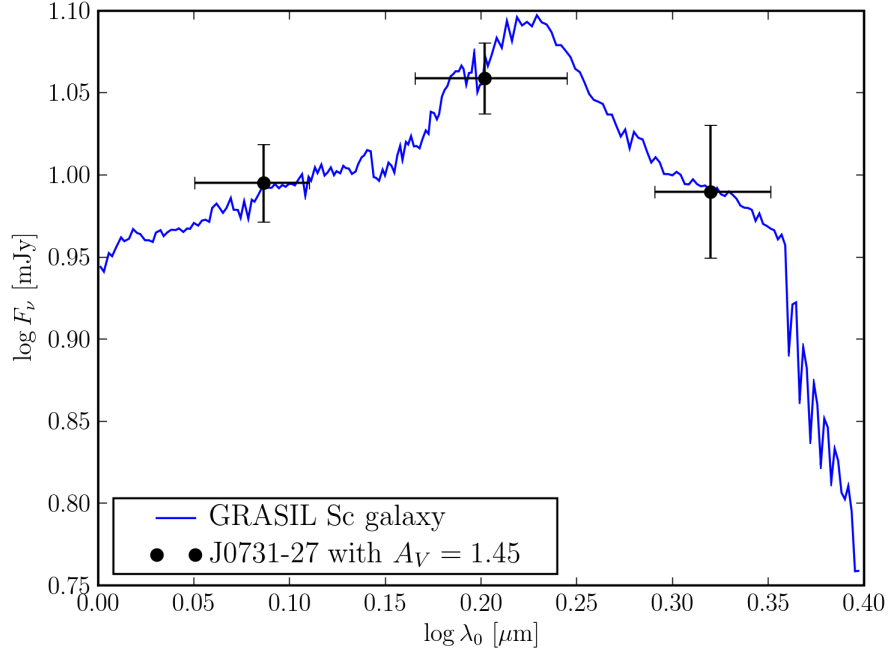


Figure 3.3: Near Infrared Spectral Energy Distribution for J0731-27, showing the extinction- and redshift-corrected flux densities in the J , H and K_s bands as well as the GRASIL template for a late-type spiral.

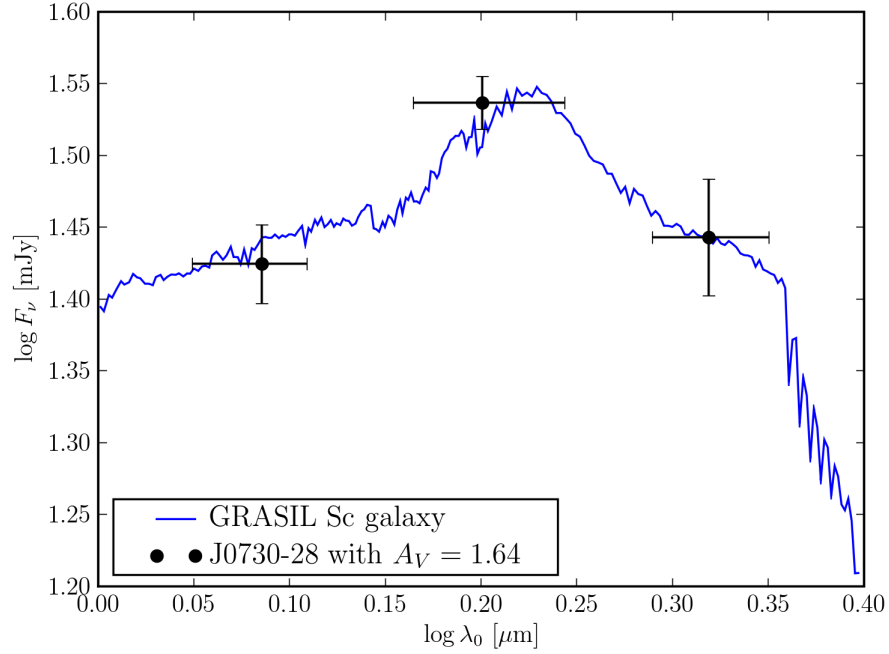


Figure 3.4: Near Infrared Spectral Energy Distribution for J0730-28, showing the extinction- and redshift-corrected flux densities in the J , H and K_s bands as well as the GRASIL template for a late-type spiral.

Chapter 4

Results and Discussion

4.1 Internal Extinction Estimate

As mentioned in §1.2.2 the Schlegel extinction values in the ZoA usually exceed the actual value by 10-30% (see for example Burstein, 2005; Dutra et al., 2002; Schröder et al., 2005). Thus, in this section we assume that the Schlegel value is 1.2 ± 0.1 times the actual Galactic extinction; then the deficit between $1/1.2$ of the Schlegel value and our fitted value, ΔA_V , can be taken as an estimate of the internal extinction. If this is a valid method we should see a correlation between the derived internal extinction and the inclination of the galaxy. These results are given in Table 4.1: the internal extinction is decomposed into the three bands using the Cardelli et al. (1989) extinction law and compared to the extinction values obtained from the relations given in Masters et al. (2003) (see §1.2.3 for a detailed description). Our results are significantly lower than the Masters values. This may be in part due to the morphology dependence of internal extinction.

Name	b/a	ΔA_V	A_{int} (Masters value)		
			J	H	K_s
		[mag]		[mag]	
J0740-22	0.500 ± 0.023	0.00 ± 0.17	0.0018	0.0012	0.0008
			0.14	0.12	0.08
J0741-30A	0.214 ± 0.008	1.05 ± 0.31	0.29	0.19	0.12
			1.31	1.14	0.87
J0731-27	0.822 ± 0.027	-0.86 ± 0.27	-0.23	-0.15	-0.10
			0.04	0.03	0.02
J0730-28	0.630 ± 0.050	0.11 ± 0.16	0.031	0.020	0.013
			0.10	0.08	0.05

Table 4.1: Estimates for the internal extinction based on the differences between the fitted extinction and the Schlegel values. The extinction values in each band derived using the relation prescribed by Masters et al. (2003) are given on the line below each galaxy. It is noted that the negative values for J0731-27 are due to the unusually high Schlegel value at $b = 4.1^\circ$.

To investigate the correlation between internal extinction and inclination, we plot the internal extinction estimate against the axis ratio, $\log(a/b)$, a proxy for galaxy inclination (Figure 4.1). The plot suggests that the internal extinction is greater for larger axis ratios, i.e. higher inclination, which adds credibility to our internal extinction estimates. We cannot, however, say anything about the nature of the relationship as this can only be done statistically and our sample is by no means large enough to constitute a statistical sample.

Furthermore, the dubious negative value for internal extinction for J0731-27 which is a result of the much higher Schlegel value ($A_V = 2.716$ mag) than our result ($A_V = 1.4 \pm 0.2$ mag), should be regarded as an outlier. This is justified since the Schlegel values for the extinction around this point vary strongly and we conclude that there is a confusion source nearby. This particular galaxy will be discussed further in §4.2.4.

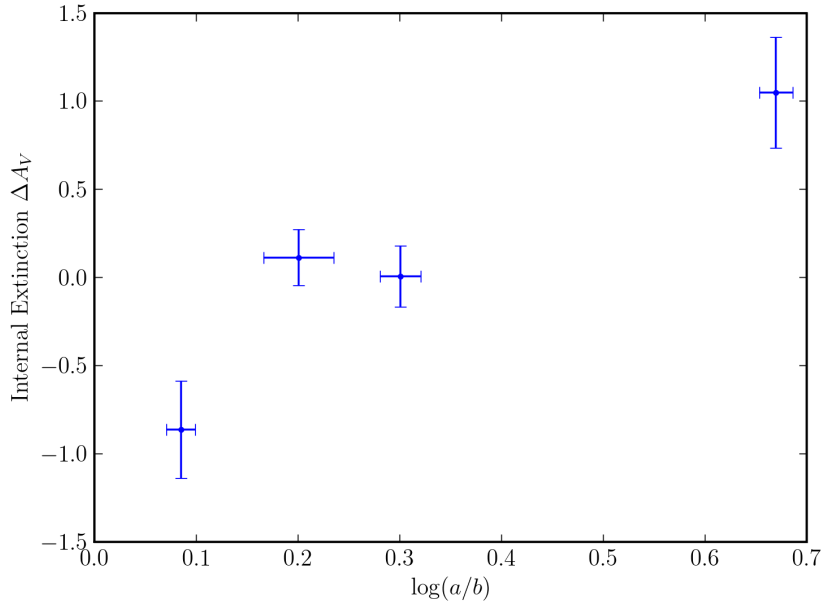


Figure 4.1: The relationship between internal extinction and the axis ratio (indirectly the inclination). The extinction is indeed larger for higher axis ratios hence inclination. The nature of the relation is indeterminate.

4.2 NIR Properties of Selected Galaxies

4.2.1 Extinction and k -corrected Magnitudes and Colours

Having obtained the total extinction we present the extinction and redshift corrected aperture magnitudes, m^o , satisfying equation 3.1 in Table 4.2 both in terms of magnitudes and flux density.

We may also now find the distance-independent colours $(J-H)^o$, $(J-K_s)^o$ and $(H-K_s)^o$. All galaxy morphologies have similar NIR colours Jarrett (2000), although the dispersion is greater for later type spirals. Moreover, the morphology-independence of NIR colours is

evident in the fact that the NIR SEDs are nearly identical for all morphologies (see Figure 1.2). Indeed, it is this very fact that we exploit in fitting the extinction to a model SED, and thus, unsurprisingly we obtain colours that are close to the standard infrared colours of unobscured galaxies $J - H = 0.68$, $J - K_s = 0.89$ and $H - K_s = 0.25$ mag (Carico et al., 1986) and agree well with the NIR color distributions of the 2MASS catalogue (Jarrett, 2000).

Name	r ["]	m_r [mag]		
		J^o	H^o	K_s^o
J0740-22	22	12.31 ± 0.10	11.74 ± 0.06	11.42 ± 0.08
J0741-30A	43	11.86 ± 0.18	11.17 ± 0.13	10.91 ± 0.13
J0731-27	23	13.03 ± 0.12	12.39 ± 0.09	12.09 ± 0.11
J0730-28	50	11.96 ± 0.09	11.19 ± 0.06	10.96 ± 0.10

Name	r ["]	F_r [mJy]		
		J^o	H^o	K_s^o
J0740-22	22	19.0 ± 1.4	20.7 ± 1.1	18.0 ± 1.4
J0741-30A	43	28.6 ± 4.8	35.0 ± 4.0	28.8 ± 3.5
J0731-27	23	9.8 ± 1.1	11.4 ± 0.9	9.7 ± 1.0
J0730-28	50	26.3 ± 2.1	34.2 ± 1.8	27.6 ± 2.6

Table 4.2: Extinction and redshift corrected apparent NIR magnitudes and flux densities enclosed in elliptical apertures with semimajor axes r .

Name	Colour [mag]		
	$(J - H)^o$	$(J - K_s)^o$	$(H - K_s)^o$
J0740-22	0.57 ± 0.10	0.89 ± 0.12	0.32 ± 0.10
J0741-30A	0.70 ± 0.22	0.95 ± 0.23	0.25 ± 0.18
J0731-27	0.65 ± 0.15	0.94 ± 0.17	0.30 ± 0.14
J0730-28	0.77 ± 0.11	1.0 ± 0.14	0.24 ± 0.12

Table 4.3: Extinction and redshift corrected NIR colours from the derived magnitudes. Compare to the galaxy colours of $J - H = 0.68$, $J - K_s = 0.89$ and $H - K_s = 0.25$ (Carico et al., 1986).

4.2.2 Disk Fitting

The surface brightness of disks of spiral galaxies follow an exponential profile

$$I = I_0 e^{-r/r_d} \quad (4.1)$$

where I is the surface brightness in intensity units, I_0 the central surface brightness, r the radius (semi-major axis) and r_d the disk scale length, the radius at which the surface

brightness is decreased by a factor of e . This may be cast in terms of magnitudes as

$$\mu = \mu_0 + 1.086 \frac{r}{r_d} \quad (4.2)$$

where $1.086 = 2.5 \log e$ and μ refers to surface brightness in magnitude units. Thus the disk part of the surface brightness (SB) profile should be linear and fitting a straight line to the disk may yield the scale length and extrapolated central surface brightness. When fitting the disk profile we restrict the semi-major axis to $r \geq 5''$ if no bulge is evident; this is ~ 3 times the width of the seeing disk (FWHM). In the case of an obvious bulge component the inner radius is determined visually. The outer radius is determined from where the K_s surface brightness reaches $22 \text{ mag arcsec}^{-2}$. The SBPs are plotted in Figures 4.2 through 4.5 with the linear fits to the disks overlaid while the disk scale lengths are given in Table 4.4. The results for the central surface brightness of the disks are given in Table 4.5. We obtain a single value for the scale length by averaging the scale lengths in the three filters. The disk scale lengths thus derived are comparable to those in the literature (for example Möllenhoff & Heidt, 2001). The angular scale is converted to physical units (kiloparsecs) by using the Hubble law

$$v = dH_0 \quad (4.3)$$

where v is the recessional velocity, obtained from the HI parameters, d is the distance and H_0 is the Hubble constant taken to be $72 \text{ km s}^{-1} \text{ Mpc}^{-1}$.*

Name	r_d [']		average [']		average [$h_{72}^{-1} \text{ kpc}$]
	J	H	K_s		
J0740-22	4.26 ± 0.03	4.08 ± 0.03	4.11 ± 0.04	4.147 ± 0.019	0.852 ± 0.004
J0741-30A	8.01 ± 0.04	8.03 ± 0.06	7.39 ± 0.08	7.796 ± 0.037	3.938 ± 0.019
J0731-27	4.34 ± 0.11	4.36 ± 0.10	4.61 ± 0.24	4.432 ± 0.089	2.179 ± 0.044
J0730-28	9.10 ± 0.11	9.68 ± 0.13	9.72 ± 0.19	9.488 ± 0.083	5.171 ± 0.045

Table 4.4: Exponential disk scale lengths.

Name	μ_0 [mag]		
	J	H	K_s
J0740-22	17.06 ± 0.02	16.21 ± 0.02	15.77 ± 0.03
J0741-30A	17.27 ± 0.01	16.35 ± 0.02	15.70 ± 0.03
J0731-27	18.70 ± 0.05	17.90 ± 0.05	17.50 ± 0.10
J0730-28	18.67 ± 0.03	17.93 ± 0.03	17.60 ± 0.04

Table 4.5: Exponential disk central surface brightnesses.

*The error in H_0 is represented by the dimensionless value h_{72} which is related to the usual Hubble parameter $h \equiv H_0/100 \text{ km s}^{-1} \text{ Mpc}^{-1}$ by $h = 0.72h_{72}$. A factor of h_{72} therefore is present in all distance dependent results.

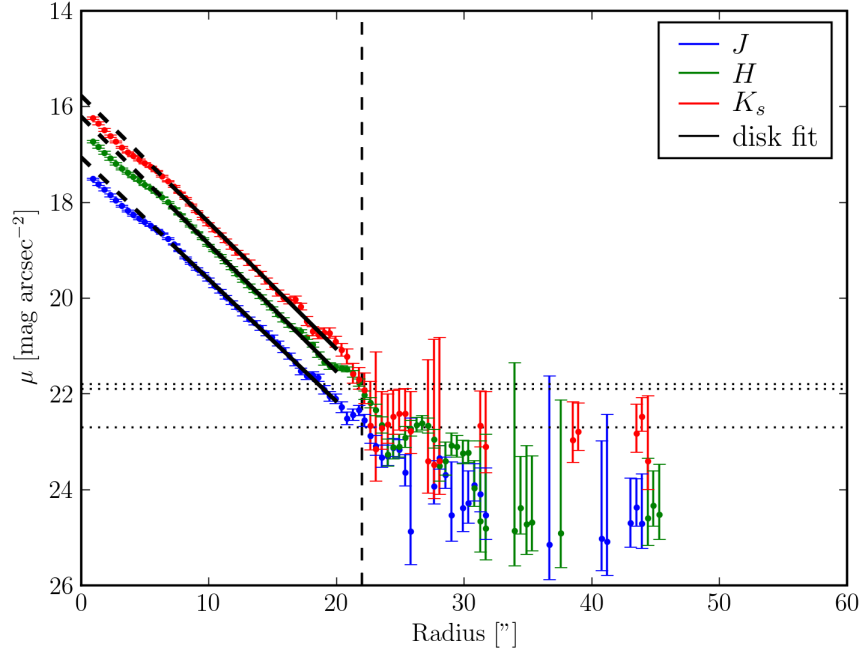


Figure 4.2: Surface brightness profiles in each band showing straight lines fitted to the disk part of J0740-22.

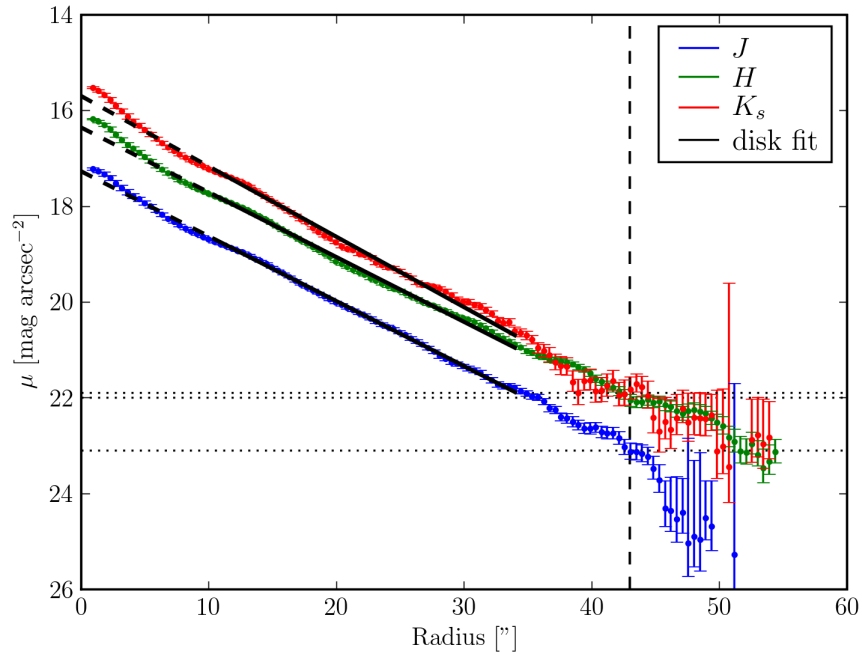


Figure 4.3: Surface brightness profiles in each band showing straight lines fitted to the disk part of J0741-30A.

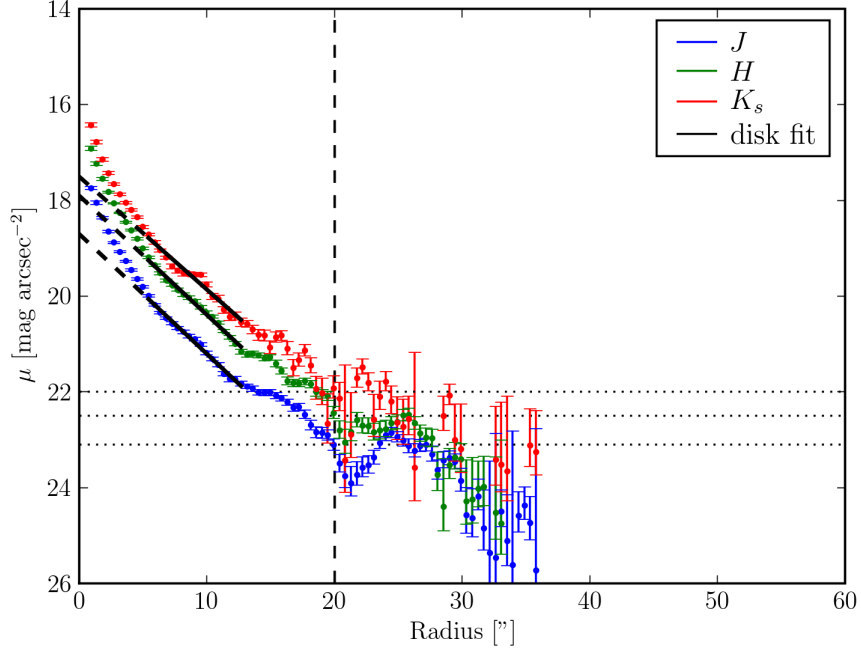


Figure 4.4: Surface brightness profiles in each band showing straight lines fitted to the disk part of J0731-27.

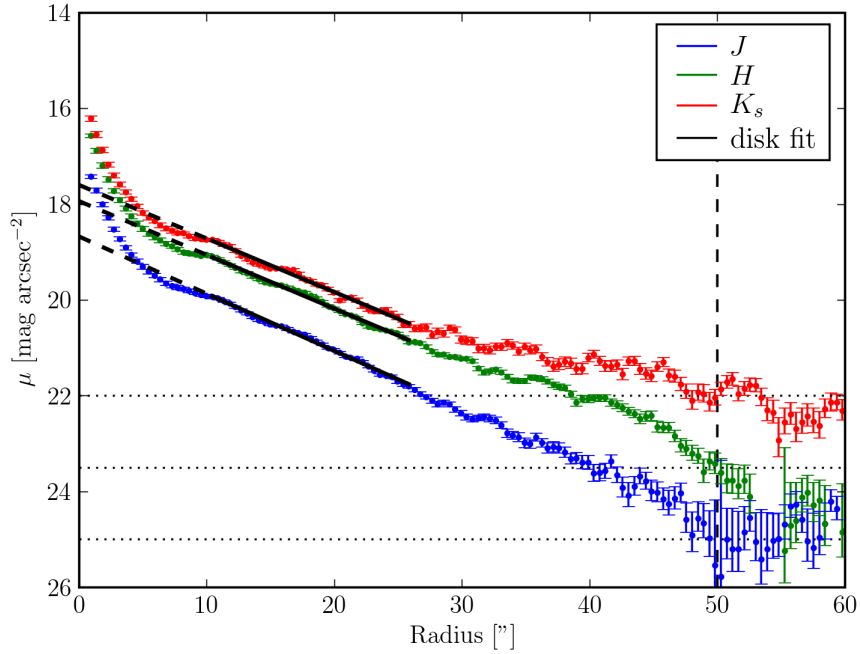


Figure 4.5: Surface brightness profiles in each band showing straight lines fitted to the disk part of J0730-28.

4.2.3 NIR Derived Parameters

HI Mass-to-Light Ratios

Given the distances based on the Hubble law (equation 4.3), we may derive other distance-dependant quantities: the absolute magnitude, hence luminosity, is found from equation 3.2. Using the HI mass and the K -band absolute magnitude of the sun, $M_{K,\odot} = 3.32$ mag (Bell et al., 2003), we calculate the K_s -band HI mass-to-light ratio in solar units. The results are given in Table 4.6. The HI mass-to-light ratio is useful as it measures the relative amounts of gas and stars in a galaxy (Kirby et al., 2008).

Name	d [h_{72}^{-1} Mpc]	$M_{K_s}^o$ [mag]	$M_{\text{HI}}/L_{K_s}^o$ [$h_{72}^2 M_{\odot}/L_{K,\odot}$]
J0740-22	42.38	-21.72	0.336
J0741-30A	104.19	-24.18	0.204
J0731-27	101.42	-22.94	0.373
J0730-28	112.40	-24.30	0.266

Table 4.6: Velocity-derived distances, absolute magnitudes in the K_s band and K_s -band HI mass-to-light ratio.

Comparison to Characteristic Luminosity

The number of galaxies with magnitude between M and $M + dM$ is quantified by the Luminosity Function $\phi(M)$

$$\phi(M) = \phi^* 10^{0.4(\alpha+1)(M^*-M)} e^{-10(0.4(M^*-M))} \quad (4.4)$$

This Schechter (1997) function has as free parameters the characteristic luminosity M^* (in magnitudes), α the faint end slope and ϕ^* the normalisation, which determine the shape of the function. Overall it has a gentle slope at the faint end and drops off suddenly at M^* . The result is that most galaxies have $M > M^*$.

While infrared galaxy surveys are less affected by systematic errors (in particular from extinction and redshift), until 2MASS, there existed few complete large galaxy samples. However, the Luminosity Function has now been determined by a number of people in the K -band. For instance, Kochanek et al. (2001) find

$$M_K^* = -24.16 \pm 0.05 \text{ mag}$$

We see that both J0741-30A and J0730-28, with $M_{K_s} = -24.18$ and -24.30 , are bright galaxies, while J0740-22 and J0731-27 are much fainter (-21.72 and -22.94 respectively). We also see that the brightness correlates with the HI mass (see Table 2.1) with the brighter galaxies being more massive.

Stellar Masses

Having obtained the K_s luminosity we may estimate the stellar masses using the relation $M/L_K = 0.95 \pm 0.03$ (Bell et al., 2003). The stellar masses thus derived are given in Table 4.7 with the HI masses for comparison. The relation between HI mass and stellar mass provides a better way to describe the relationship between the gas and stellar content of a galaxy (Kirby et al., 2008). The HI mass is plotted as a function of stellar mass in Figure 4.6; the HI mass generally increases with increasing stellar mass. This is supported in the literature, where an upper envelope to a galaxy’s mass-to-light ratio at a given luminosity is proposed (Kirby et al., 2008).

Name	M_{HI} [$10^9 \mathcal{M}_\odot$]	M_* [$10^9 \mathcal{M}_\odot$]	M_*/M_{HI}
J0740-22	3.47	9.77	2.81
J0741-30A	20.4	94.6	4.64
J0731-27	11.9	30.5	2.56
J0730-28	29.6	106	3.58

Table 4.7: Comparison of stellar and HI masses.

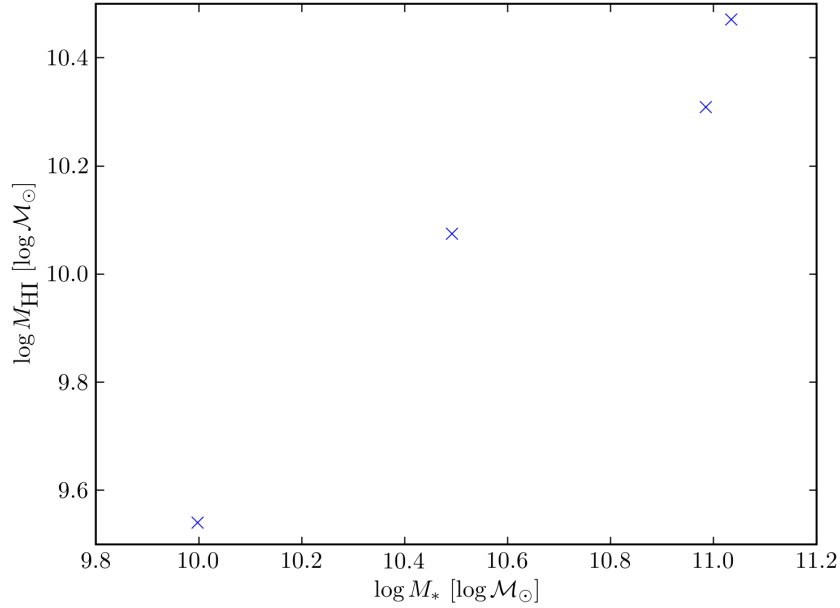


Figure 4.6: HI mass versus stellar mass

4.2.4 J0731-27

This galaxy is not detected in 2MASS and is an obvious outlier in the internal extinction plot. The three-colour IRSF image is shown in Figure 4.7 (see also the HI profile in Figure A.3). It is relatively small ($r_d = 2.18$ kpc) and faint ($M_{K_s} = -22.94$ mag), and has the

lowest stellar mass to HI mass ($M_*/M_{\text{HI}} = 2.56$) of the four galaxies. Consideration of all these values, including the IRSF image and HI profile, suggest that this is a late-type spiral or irregular galaxy.

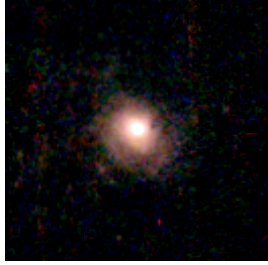


Figure 4.7: $1' \times 1'$ IRSF image for J0731-27.

4.3 2MASS Counterparts

4.3.1 Comparison

We searched NED[†] for 2MASS counterparts to our galaxies. Three of the galaxies have 2MASS counterparts: J0740-22, J0741-30A and J0730-28. J0731-27 is not seen by 2MASS. We compare here the results obtained by 2MASS with our results. Each galaxy is discussed separately in the following subsections. Comparison of the 2MASS and IRSF images (Figures 4.8 through 4.10) clearly show the improved resolution of IRSF over 2MASS. The photometry is compared in Tables 4.8 through 4.10; we obtain comparable magnitudes and errors as well as apertures. The 2MASS magnitudes quoted here are extrapolated total magnitudes, while the IRSF magnitudes are the total magnitudes (returned by `radprofil`) which have been transformed to the 2MASS system (via equations 2.1).

J0740-22

Figure 4.8 shows J0740-22 and its 2MASS counterpart 2MASX J07405956-2255444. A comparison of the photometry is given in Table 4.8.

	ϵ	ϕ [deg]	r ["]	J^o [mag]	H^o [mag]	K_s^o [mag]
2MASS	0.3	-15	22.73	12.86 ± 0.07	11.91 ± 0.05	11.66 ± 0.08
IRSF	0.5	-18	23	12.78 ± 0.07	11.98 ± 0.04	11.54 ± 0.09

Table 4.8: Comparison of 2MASS and IRSF magnitudes for J0740-22

[†]The NASA/IPAC Extragalactic Database (NED) is operated by the Jet Propulsion Laboratory, California Institute of Technology, under contract with the National Aeronautics and Space Administration

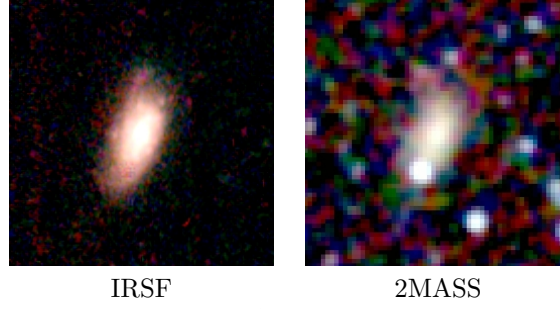


Figure 4.8: Comparison of IRSF and 2MASS images for J0740-22. The images are both $1' \times 1'$.

J0741-30A

Figure 4.9 shows J0741-30A and its 2MASS counterpart 2MASX J07414792-3028212. A comparison of the photometry is given in Table 4.9.

	ϵ	ϕ [deg]	r [']	J^o [mag]	H^o [mag]	K_s^o [mag]
2MASS	0.76	80	45.63	12.44 ± 0.06	11.60 ± 0.05	11.06 ± 0.07
IRSF	0.79	82.9	43	12.57 ± 0.06	11.46 ± 0.04	11.06 ± 0.07

Table 4.9: Comparison of 2MASS and IRSF magnitudes for J0741-30A

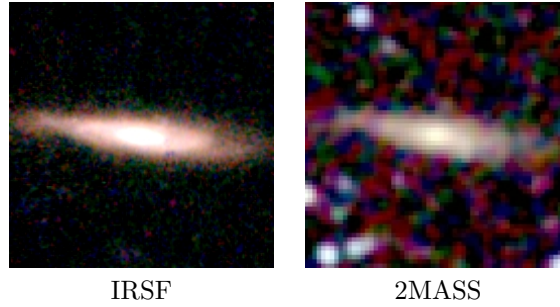


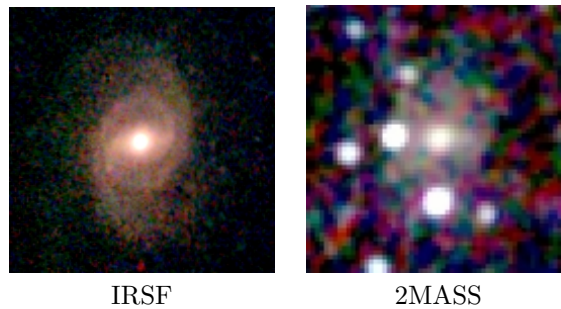
Figure 4.9: Comparison of IRSF and 2MASS images for J0741-30A. The images are both $1' \times 1'$.

J0730-28

Figure 4.10 shows J0730-28 and its 2MASS counterpart 2MASX J07304535-2823585. A comparison of the photometry is given in Table 4.10. The discrepancy in the ellipse parameters is explained by the fact that the 2MASS ellipse is fit much closer to the center of the galaxy, while ours is fit further out. This galaxy was poorly fit by `ellipse` due to its spiral structure, thus we estimated by eye the ellipse parameters.

	ϵ	ϕ [deg]	r [$''$]	J^o [mag]	H^o [mag]	K_s^o [mag]
2MASS	0.12	-40	45.57	11.60 ± 0.07	10.94 ± 0.07	10.47 ± 0.10
IRSF	0.37	2	50	12.32 ± 0.07	11.42 ± 0.04	10.88 ± 0.09

Table 4.10: Comparison of 2MASS and IRSF magnitudes for J0730-28

Figure 4.10: Comparison of IRSF and 2MASS images for J0730-28. The images are both $1' \times 1'$.

Chapter 5

Conclusion

5.1 Summary of Results

The high extinction and stellar density at low Galactic latitude results in optical and near infrared surveys becoming incomplete close to the Galactic Plane and Galactic Bulge. The 21 cm line of neutral hydrogen has by far proven to be the most effective at penetrating this Zone of Avoidance. It provides, however, little information about the nature of the galaxies. Data from other wavelengths are required for determination of the properties of the galaxies. The NIR is well suited to this as it is both able to penetrate the dust of the Milky Way and it traces out the old stellar population, hence provides a good estimate of the mass of the galaxy.

As part of an ongoing follow up programme of NIR observations of galaxies discovered in the HI Parkes deep Zone of Avoidance survey, we have studied the NIR properties of four of these galaxies.

- ★ From Spectral Energy Density fitting we determine the total extinction (internal and Galactic) in the direction of each galaxy. We find values ranging from 1.4 to 2.2 mag, which are not inconsistent with the Schlegel values. Moreover we exploit the $\sim 10 - 30\%$ discrepancy between the Schlegel values and the actual extinction in the ZoA to determine an estimate of the internal extinction for each galaxy. As expected, this correlates with the axis ratio or inclination.
- ★ Taking the extinction and k -corrections into account, we determined the extinction-corrected magnitudes and NIR colours, the latter being consistent with the known NIR colours of unobscured galaxies.
- ★ By fitting an exponential profile to the disk parts of the galaxies we determined the disk scale lengths and central disk brightness. Scale lengths vary from $\sim 1 - 5 h_{72}^{-1}$ kpc.
- ★ Using the redshift to estimate a distance we obtained the K_s -band luminosities. Two of the galaxies are L^* galaxies, while the other two $\sim 1 - 2$ mag fainter. Assuming a stellar mass to light ratio we determined the stellar masses of the galaxies. We obtain

masses of $\sim 10 - 100 \times 10^9 \mathcal{M}_{\odot}$ with the more massive ones being brighter and having greater HI masses.

- ★ For the three galaxies with 2MASS counterparts, we compare our results to the 2MASS results and show that our photometry is consistent with 2MASS.

5.2 Future Prospects

This work demonstrates the usefulness of NIR imaging. It provides complementary data to the HI data. Over a thousand galaxies were discovered in the HIZOA survey, many of which have already been observed by our group with the IRSF telescope under the same conditions as the four galaxies discussed in this project. These observations remain to be reduced and analysed. This data will be useful in a number of applications, for example

- ★ A number of dynamically interesting structures lie behind the ZoA, in particular the Local Void. One can study the nature of the galaxies in and near the Local Void to determine if they are different from other galaxies.
- ★ The details on luminosity and inclination provided by the NIR imaging can be combined with the velocity width of the HI data and used with the Tully-Fisher relation to determine independent distances. This can in turn be used to determine peculiar velocities and thereby the mass distribution in the ZoA.
- ★ In regions of overlap with the Galactic Legacy Infrared Mid-Plane Survey Extraordinaire (GLIMPSE) by the Spitzer Telescope in the Mid Infrared, we should be able to detect these galaxies, in which case we can use the MIR information to extend the SEDs and investigate other parameters such as the star formation rate.

Appendix A

HI Spectra

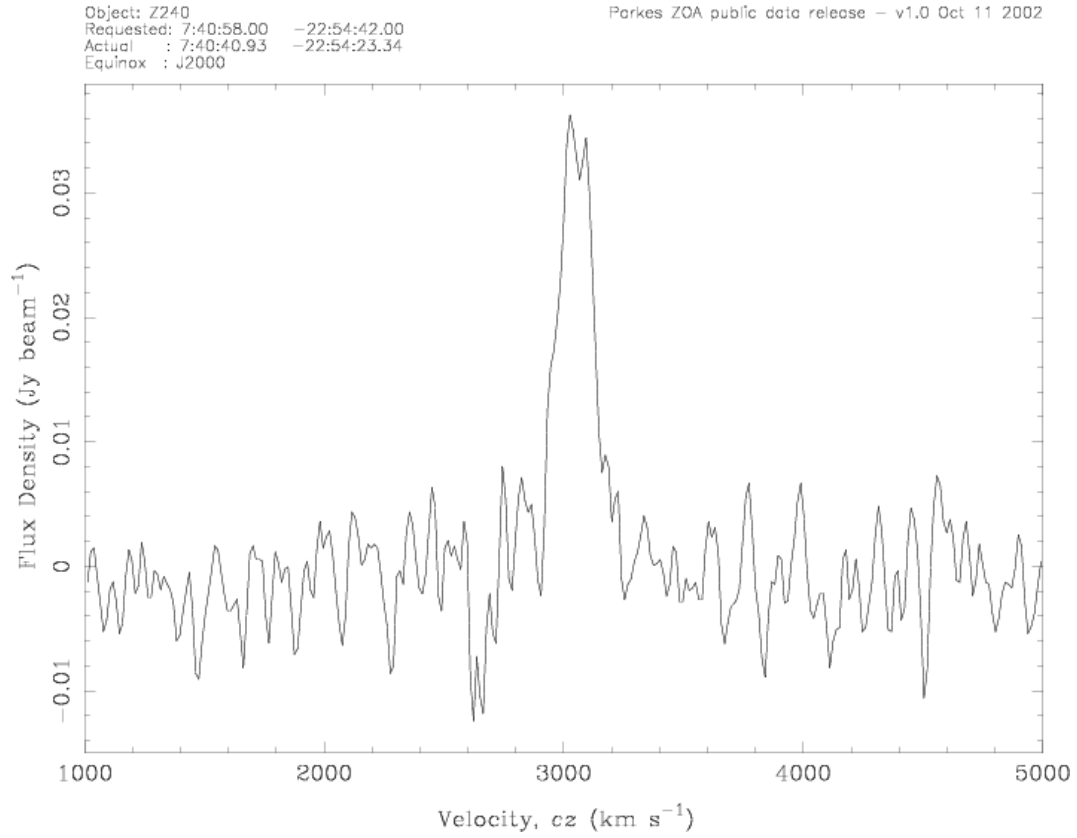


Figure A.1: HIZOA spectrum for J0740-22 giving a velocity of 3051 km s^{-1} and HI mass of $3.47 \times 10^9 \mathcal{M}_{\odot}$.

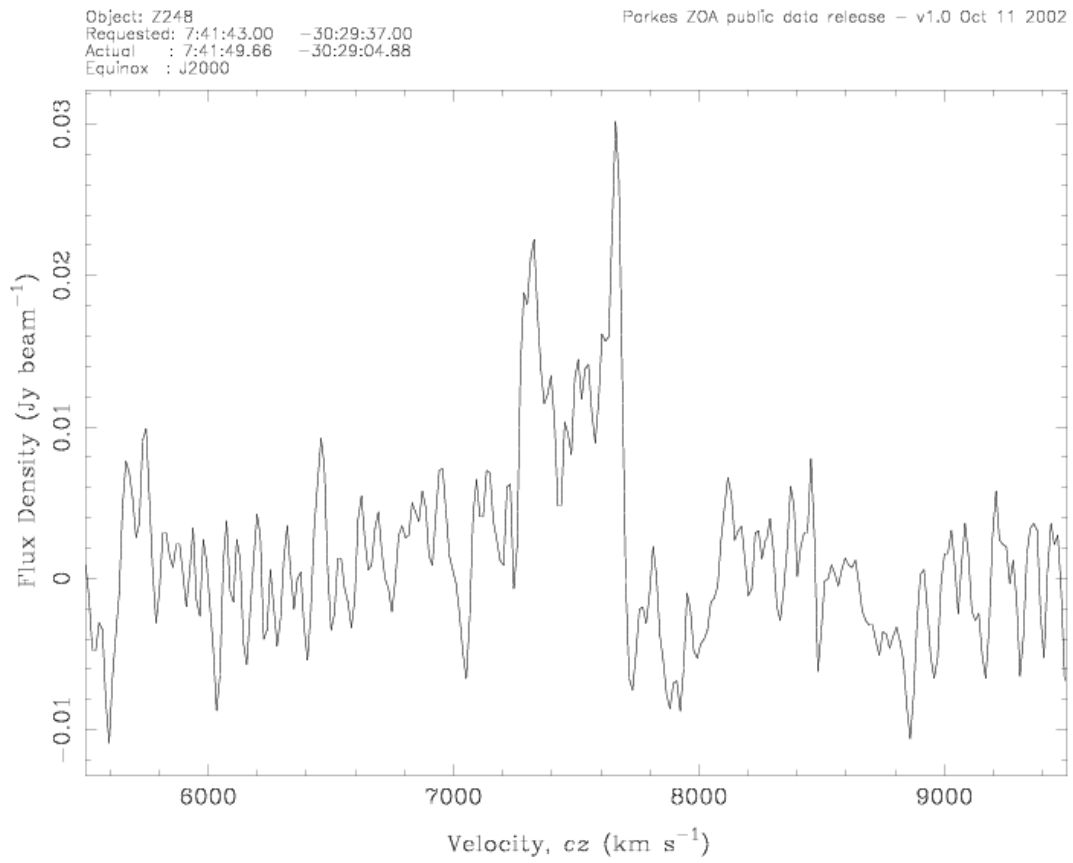


Figure A.2: HIZOA spectrum for J0741-30A giving a velocity of 7502 km s^{-1} and HI mass of $20.4 \times 10^9 \mathcal{M}_{\odot}$.

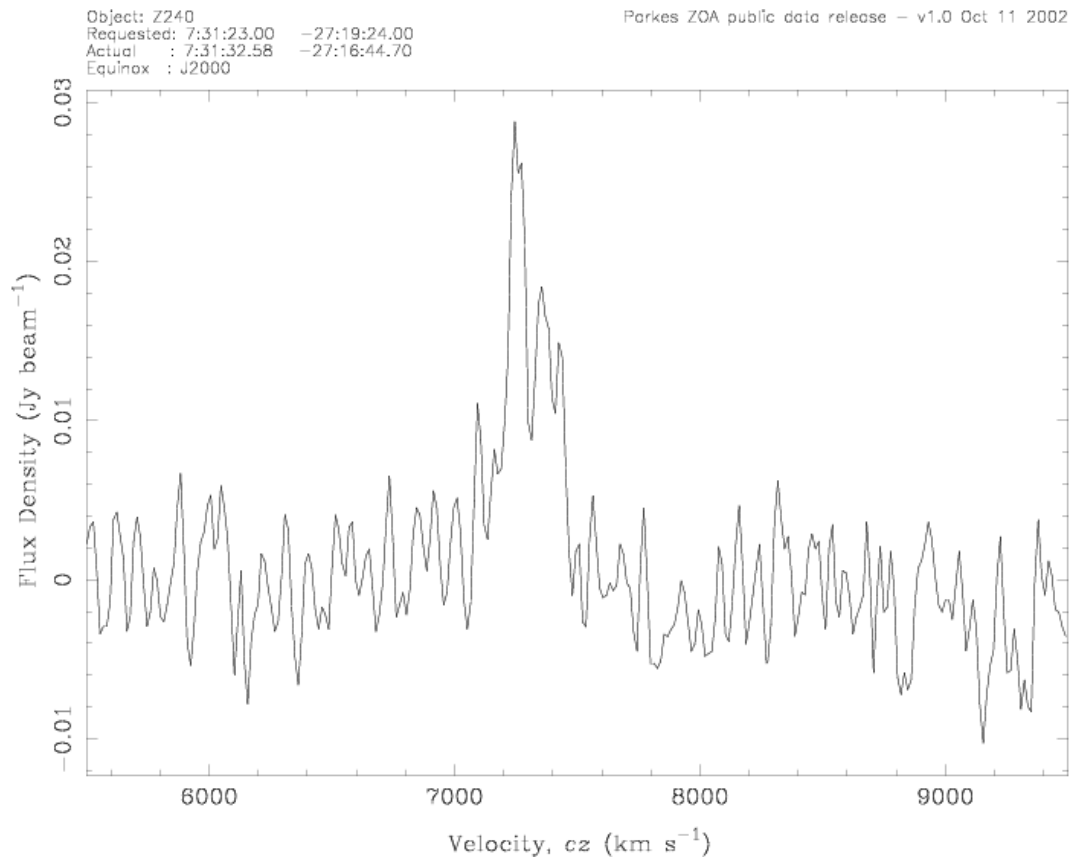


Figure A.3: HIZOA spectrum for J0731-27 giving a velocity of 7302 km s^{-1} and HI mass of $11.9 \times 10^9 \mathcal{M}_{\odot}$.

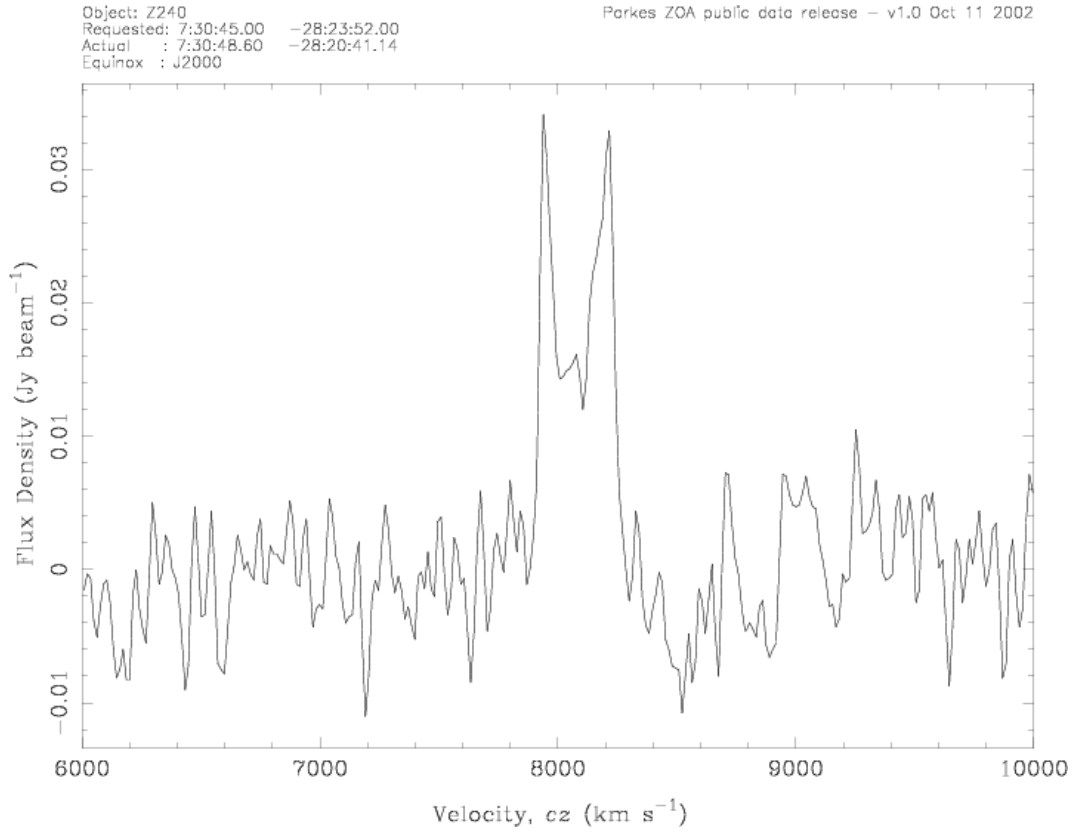


Figure A.4: HIZOA spectrum for J0730-28 giving a velocity of 8093 km s^{-1} and HI mass of $29.6 \times 10^9 \mathcal{M}_{\odot}$.

Appendix B

HI Lists

The list of HIZOA galaxies that have been observed on the IRSF. Some of the coordinates were updated with the optimised values from the HIZOA spectra. Some of the original HI coordinates had errors $> 4'$ and thus may have been missed in the IRSF observations. Comparison of the old and new coordinates allows us to flag the galaxies with deviations of $> 4'$.

Column 1 HIZOA Name

Columns 2 and 3 Equatorial Coordinates (J2000): Right Ascension (RA) and Declination (Dec)

Columns 4 and 5 Galactic coordinates: Galactic latitude (b) and Galactic longitude (l)

Column 6 Heliocentric velocity (V), measured at 50% of the profile's peak flux

Column 7 Integrated HI flux (S)

Column 8 HI mass* (M_{HI})

Column 9 Colour excess ($E(B - V)$) from Schlegel et al. (1998)

Column 10 Observation date

Column 11 Seeing: '1' - good to satisfactory quality; '3' - borderline good (e.g. reasonable seeing but high stellar density); '5' - good seeing but cirrus/clouds; '7' - borderline, should be reobserved; and '9' - unacceptable, must be reobserved

Column 12 Updated, marked with a "y" if the coordinates were updated with optimised HI coordinates

* $M_{\text{HI}} = 2.356 \times 10^5 D^2 \int S dv M_{\odot}$ where D is the distance to the galaxy in Mpc, S is the specific flux and the integral is over the velocity width of the galaxy.

Table B.1: Parameters for HIZOA galaxies observed with the IRSF.

name	RA [hh mm ss]	Dec [° ' '']	l [deg]	b [deg]	v [km s ⁻¹]	S [Jy km s ⁻¹]	M_{HI} [10 ⁹ M _⊙]	$E(B-V)$ [mag]	obs date [date]	seeing	updated
J0657-05A	06 57 41.44	-05 14 10.9	218.3042	-0.9991	2628	28.6	7.28	1.22926	12/04/07	9	
J0657-05B	06 57 58.02	-05 19 21.9	218.4125	-0.9773	2720	27.2	7.42	1.26448	12/04/07	9	
J0701+01	07 01 04.24	+01 54 01.8	212.3372	3.0094	1738	15.5	2.66	0.52731	12/04/07	9	
J0701-07	07 01 58.52	-07 18 37.8	220.6360	-0.9997	1749	3.1	0.448	1.05562	12/04/07	9	
J0730-11	07 30 01.32	-11 12 48.9	227.3167	3.3026	2423	1.0	0.195	0.29149	16/04/07	1	
J0730-17	07 30 31.18	-17 17 20.3	232.7110	0.4982	1657	1.3	0.161	1.13619	16/04/07	1	
J0730-22	07 30 09.65	-22 00 35.6	236.8128	-1.8415	773	87.9	2.64	1.60238	16/04/07	1	
J0730-25	07 30 23.26	-25 06 56.5	239.5679	-3.2817	8424	2.9	8.19	0.96950	16/04/07	1	
J0730-28	07 30 45.23	-28 23 52.0	242.4999	-4.7733	8093	10.8	29.6	0.54269	16/04/07	1	
J0731-23	07 31 23.15	-23 32 59.9	238.3006	-2.3323	2993	4.2	1.67	0.79798	16/04/07	1	
J0731-27	07 31 22.52	-27 19 23.9	241.6177	-4.1409	7302	5.4	11.9	0.86633	16/04/07	1	
J0732-16	07 32 07.14	-16 58 16.6	232.6164	0.9861	4320	1.2	0.948	4.26074	16/04/07	1	
J0732-28	07 32 40.71	-28 21 11.8	242.6631	-4.3799	8018	3.7	10.1	0.64586	16/04/07	1	
J0733-08	07 33 36.36	-08 24 59.1	225.2739	5.4132	8968	6.1	19.8	0.20762	17/04/07	1	
J0733-13	07 33 32.19	-13 56 32.7	230.1264	2.7460	3253	2.6	1.30	0.50117	17/04/07	1	
J0733-28	07 33 14.58	-28 40 12.9	243.0017	-4.4228	2095	10.5	2.07	0.58305	17/04/07	1	
J0734-14	07 34 02.69	-14 41 28.9	230.8425	2.4923	3295	6.8	3.56	0.60709	17/04/07	1	
J0735-17	07 35 59.02	-17 17 52.2	233.3495	1.6356	3244	4.3	1.88	0.89739	17/04/07	1	
J0736-18	07 36 37.91	-18 05 02.3	234.1115	1.3875	4463	3.2	2.74	0.95300	17/04/07	1	
J0737-31	07 37 10.15	-31 06 00.7	245.5497	-4.8458	2247	5.0	1.08	0.53814	17/04/07	1	

Continued on Next Page...

Table B.1 – Continued

name	RA [hh mm ss]	Dec [° ' '']	l [deg]	b [deg]	v [km s ⁻¹]	S [Jy km s ⁻¹]	M_{HI} [10 ⁹ M _⊙]	$E(B - V)$ [mag]	obs date [date]	seeing	updated
J0738-15	07 38 58.22	-15 30 31.2	232.1362	3.1339	884	2.6	0.106	0.63168	18/04/07	7	
J0738-16	07 38 01.65	-16 57 40.5	233.2938	2.2261	3171	15.7	6.07	0.63391	18/04/07	7	
J0738-24	07 38 11.49	-24 37 43.2	239.9981	-1.4969	5461	2.1	2.64	0.85744	17/04/07	1	
J0738-26	07 38 51.41	-26 12 24.4	241.4481	-2.1393	2963	8.1	2.84	0.88067	18/04/07	7	
J0739-23	07 39 40.11	-23 16 00.7	238.9774	-0.5342	3124	2.5	1.06	0.66718	18/04/07	9	
J0739-24	07 39 52.13	-24 42 09.0	240.2496	-1.2012	3055	13.7	5.74	0.77674	20/04/07	1	
J0739-26A	07 39 03.34	-26 19 47.4	241.5773	-2.1608	3419	3.7	1.76	0.87348	18/04/07	7	
J0739-26B	07 39 46.11	-26 30 49.1	241.8160	-2.1120	3557	2.2	1.16	0.80367	18/04/07	7	
J0740-22	07 40 58.27	-22 54 42.1	238.8163	-0.0984	3051	8.8	3.47	0.61152	21/04/07	1	
J0740-30A	07 40 15.80	-30 57 23.0	245.7469	-4.1967	5079	10.2	10.60	0.47671	20/04/07	1	
J0740-30B	07 40 50.10	-30 49 50.5	245.6973	-4.0282	7449	7.6	17.1	0.47991	20/04/07	1	
J0740-32	07 40 49.33	-32 03 20.9	246.7672	-4.6305	2723	12.5	3.81	0.64753	20/04/07	1	
J0741-22	07 41 43.26	-22 31 13.8	238.5619	0.2455	3068	35.7	13.6	0.76230	21/04/07	1	
J0741-25	07 41 38.32	-25 43 01.9	241.3300	-1.3540	7810	6.2	16.0	0.79209	21/04/07	1	
J0741-26	07 41 58.42	-26 04 51.2	241.6834	-1.4686	3506	2.3	1.19	0.80285	21/04/07	1	
J0741-30A	07 41 42.71	-30 29 36.7	245.4958	-3.6983	7502	8.9	20.4	0.54966	21/04/07	1	
J0741-30B	07 41 57.86	-30 10 44.4	245.2484	-3.4960	4558	9.1	7.72	0.59106	21/04/07	1	
J0741-30C	07 41 42.87	-30 55 33.2	245.8733	-3.9105	1890	3.0	0.377	0.46512	21/04/07	1	
J0742-20A	07 42 39.76	-20 27 52.1	236.8849	1.4553	10097	1.5	6.36	0.58326	22/04/07	5	
J0742-20B	07 42 57.25	-20 16 26.8	236.7536	1.6091	10241	4.4	19.4	0.83862	22/04/07	5	
J0742-26	07 42 04.45	-26 43 14.2	242.2505	-1.7658	2913	7.2	2.59	0.93726	22/04/07	5	

Continued on Next Page...

Table B.1 – Continued

name	RA [hh mm ss]	Dec [° ' '']	l [deg]	b [deg]	v [km s ⁻¹]	S [Jy km s ⁻¹]	M_{HI} [10 ⁹ M _⊙]	$E(B - V)$ [mag]	obs date [date]	seeing	updated
J0742-31	07 42 51.71	-31 58 59.1	246.9165	-4.2182	2103	34.8	5.64	0.93960	22/04/07	5	
J0742-34	07 42 34.12	-34 36 51.0	249.1864	-5.5641	2895	39.6	12.1	1.62098	22/04/07	5	
J0743-18	07 43 33.91	-18 14 39.5	235.0621	2.7423	3338	5.8	2.47	0.56309	23/04/07	1	
J0743-25A	07 43 25.56	-25 55 39.6	241.7124	-1.1092	2772	4.4	1.44	0.84358	23/04/07	1	
J0743-25B	07 43 18.06	-25 45 04.1	241.5453	-1.0458	7088	12.8	27.3	0.64429	23/04/07	1	
J0743-32	07 43 00.77	-32 34 56.6	247.4553	-4.4857	6369	3.5	5.86	1.02292	22/04/07	5	
J0744-13	07 44 29.52	-13 03 57.8	230.6608	5.4985	2307	26.1	4.83	0.35171	23/04/07	1	
J0744-25	07 44 26.35	-25 59 20.3	241.8791	-0.9424	4049	3.6	2.48	1.02241	23/04/07	1	
J0744-26	07 44 23.41	-26 01 48.4	241.9093	-0.9725	2724	10.4	3.23	1.02241	23/04/07	1	
J0744-27	07 44 55.38	-27 21 10.1	243.1149	-1.5300	7246	3.2	7.01	0.79557	24/04/07	7	
J0744-31	07 44 22.16	-31 30 42.2	246.6648	-3.7065	3135	2.0	0.696	0.91567	23/04/07	1	
J0900-39	09 00 31.31	-39 26 09.6	262.0126	4.4366	2627	13.4	4.11	0.61872	14/04/07	5	
J0901-41	09 01 35.17	-41 14 27.7	263.5091	3.4020	5094	2.5	2.83	1.09081	14/04/07	5	
J0902-40	09 02 00.34	-40 07 20.4	262.7191	4.1998	1634	12.5	1.64	0.52224	14/04/07	5	
J0903-41	09 03 22.15	-41 18 47.0	263.7852	3.6055	5442	7.7	9.65	1.19404	14/04/07	5	
J0904-45	09 04 19.98	-45 16 48.6	266.8651	1.0955	7216	2.6	5.71	2.55366	14/04/07	5	
J0905-44	09 05 02.04	-44 43 19.6	266.5327	1.5606	7104	4.7	9.94	2.63166	14/04/07	7	
J0905-46	09 05 17.29	-46 15 22.9	267.7025	0.5666	7448	6.2	13.8	1.45987	14/04/07	5	
J0907-42	09 07 38.89	-42 28 35.0	265.1852	3.4194	2304	1.3	0.224	0.84069	14/04/07	5	
J0907-48	09 07 09.05	-48 16 54.0	269.4145	-0.5606	5219	5.1	5.43	2.81238	14/04/07	7	
J1246-63	12 46 25.33	-63 03 41.6	302.3639	-0.1953	3873	83	14.7	5.14163	16/04/07	1	y

Continued on Next Page...

Table B.1 – Continued

name	RA [hh mm ss]	Dec [° ' '']	l [deg]	b [deg]	v [km s ⁻¹]	S [Jy km s ⁻¹]	M_{HI} [10 ⁹ M_{\odot}]	$E(B - V)$ [mag]	obs date [date]	seeing	updated
J1320-63	13 20 09	-63 17 32	306.15	-0.60	3682	24	3.05	4.76893	16/04/07	1	y
J1326-61	13 26 57.00	-61 37 26.0	307.1388	0.9574	6360	42	9.84	3.02535	16/04/07	1	y
J1604-41	16 04 44.91	-41 43 35.4	337.1867	7.9398	4575	56	12.3	0.77153	24/04/07	5	y
J1610-38	16 10 31.28	-38 20 26.0	340.3370	9.6699	4428	58	5.61	0.73293	24/04/07	5	y
J1620-39	16 20 30.47	-39 36 24.3	340.8438	7.4075	2384	92	3.26	0.83044	24/04/07	5	y [†]
J1623-40	16 23 43.37	-40 39 3.4	340.5284	6.2370	4700	88	4.57	1.17817	24/04/07	5	y
J1624-42	16 24 42.97	-42 30 09.3	339.3269	4.8112	2215	22.8	4.69	1.06354	13/04/07	7	
J1629-26	16 29 46.93	-26 45 13.1	351.7546	14.7889	4988	48	13.8	0.48021	24/04/07	5	y
J1643-54	16 43 15.90	-54 08 43.1	332.8431	-5.3363	5220	7.3	8.24	0.33428	13/04/07	7	
J1653-35	16 53 39.7	-35 37 56	348.2217	5.1597	6328	17.6	30.1	1.01306	13/04/07	7	
J1658-30*	16 58 41.78	-30 38 22.5	352.8200	7.4287	2769	34	1.49	0.41826	21/04/07	1	y
J1704-33B	17 04 32.04	-33 12 03.7	351.5303	4.8888	6206	7.0	11.2	0.52543	13/04/07	7	
J1705-27	17 05 32.20	-27 07 58.1	356.5563	8.3461	7990	43	12.6	0.32017	24/04/07	5	y
J1708-31	17 08 37.12	-31 20 33.9	353.5439	5.3078	6910	40	11.8	0.68204	24/04/07	5	y
J1711-47	17 11 35.96	-47 39 21.7	340.7271	-4.8218	2184	17.4	3.58	0.71202	13/04/07	7	
J1719-45	17 19 19.19	-45 55 20.5	342.9134	-4.8980	5793	4.8	6.69	0.55167	13/04/07	7	
J1722-32	17 22 40.39	-32 16 11.8	354.5200	2.3367	6211	21.5	33.7	2.43659	13/04/07	7	
J1736-47	17 36 46.93	-47 50 36.0	342.9355	-8.4457	5620	51	19.4	0.24183	24/04/07	5	y
J1749-15	17 49 21.58	-15 20 45.8	12.1197	6.2558	7266	39	14.9	0.66362	24/04/07	5	y [†]
J1734-16*	17 34 23.66	-16 45 21.1	9.0300	8.6072	1404	45	0.207	0.45149	20/04/07	1	y
J1757-04*	17 57 57.12	-04 03 33.2	23.0997	9.9640	1721	38	0.319	1.18533	15/04/07	1	y

Continued on Next Page...

Table B.1 – Continued

name	RA [hh mm ss]	Dec [° ' '']	l [deg]	b [deg]	v [km s ⁻¹]	S [Jy km s ⁻¹]	M_{HI} [10 ⁹ M _⊙]	$E(B - V)$ [mag]	obs date [date]	seeing	updated
J1807-08	18 07 24.62	-08 39 20.7	20.1582	5.7024	3554	90	17.7	1.35948	24/04/07	5	y [†]
J1824-01A	18 24 31.71	-01 55 36.9	28.1339	5.0985	6098	58	12.5	1.85580	24/04/07	5	y
J1814-02*	18 14 31.40	-02 27 10.6	26.5011	7.0703	1714	74	2.71	2.04510	15/04/07	1	y
J1817-03*	18 17 50.94	-03 17 07.2	26.1483	5.9480	1856	44	0.625	1.93543	15/04/07	1	y
J1817-32*	18 17 31.74	-32 08 20.8	0.5869	-7.5550	972	28	0.0107	0.25822	20/04/07	1	y [†]
J1819-01*	18 19 02.93	-01 07 20.8	28.2164	6.6846	2936	52	2.24	1.12104	15/04/07	1	y
J1826+01*	18 26 38.55	+01 33 33.9	31.4909	6.2274	2734	46	1.61	1.47263	20/04/07	1	y
J1826+03*	18 26 37.54	+03 04 25.7	32.8467	6.9198	2919	56	1.95	0.73558	21/04/07	1	y
J1827+04*	18 27 53.34	+04 07 14.0	33.9309	7.1124	2019	29	0.840	0.39450	21/04/07	1	y
J1828-33*	18 28 27.42	-33 10 44.7	0.6905	-10.0770	692	43	0.0326	0.17061	20/04/07	1	y
J1901-04	19 01 47.30	-04 30 09.6	30.0953	-4.3504	1523	106	1.22	0.80789	24/04/07	5	y

NOTES:

* Local Void galaxies

† change in declination larger than 4' (half the field of view)

Bibliography

- Bell, E. F., McIntosh, D. H., Katz, N., & Weinberg, M. D. 2003, *ApJS*, 149, 289
- Bruzual, A. G. 1983, *ApJ*, 273, 105
- Bruzual, A. G. & Charlot, S. 1993, *ApJ*, 405, 538
- Burstein, D. 2005, in *Astronomical Society of the Pacific Conference Series*, Vol. 329, *Nearby Large-Scale Structures and the Zone of Avoidance*, ed. A. P. Fairall & P. A. Woudt, 111
- Burstein, D. & Heiles, C. 1982, *AJ*, 87, 1165
- Cardelli, J. A., Clayton, G. C., & Mathis, J. S. 1989, *ApJ*, 345, 245
- Carico, D. P., Soifer, B. T., Beichman, C., Elias, J. H., Matthews, K., & Neugebauer, G. 1986, *AJ*, 92, 1254
- Charlot, S. & Bruzual, A. G. 1991, *ApJ*, 367, 126
- Cluver, M. E., Jarrett, T. H., Appleton, P. N., Kraan-Korteweg, R. C., Woudt, P. A., Koribalski, B. S., Donley, J. L., Wakamatsu, K., & Nagayama, T. 2008, *ApJ*, 686, L17
- Cohen, M., Wheaton, W. A., & Megeath, S. T. 2003, *AJ*, 126, 1090
- Donley, J. L., Staveley-Smith, L., Kraan-Korteweg, R. C., Islas-Islas, J. M., Schröder, A., Henning, P. A., Koribalski, B., Mader, S., & Stewart, I. 2005, *AJ*, 129, 220
- Dutra, C. M., Santiago, B. X., & Bica, E. 2002, *A&A*, 381, 219
- Epchtein, N., de Batz, B., Capoani, L., Chevallier, L., Copet, E., Fouqué, P., Lacombe, P., Le Bertre, T., et al. 1997, *The Messenger*, 87, 27
- Ewen, H. I. & Purcell, E. M. 1951, *Nature*, 168
- Glass, I. S. 1999, *Handbook of Infrared Astronomy* (Cambridge University Press)
- Henning, P. A., Kraan-Korteweg, R. C., Rivers, A. J., Loan, A. J., Lahav, O., & Burton, W. B. 1998, *AJ*, 115, 584

- Henning, P. A., Kraan-Korteweg, R. C., & Staveley-Smith, L. 2005, in *Astronomical Society of the Pacific Conference Series*, Vol. 329, *Nearby Large-Scale Structures and the Zone of Avoidance*, ed. A. P. Fairall & P. A. Woudt, 199
- Hogg, D. W., Baldry, I. K., Blanton, M. R., & Eisenstein, D. J. 2002, arXiv e-prints
- Humason, M. L., Mayall, N. U., & Sandage, A. R. 1956, *AJ*, 61, 97
- Jarrett, T. 2004, *Publications of the Astronomical Society of Australia*, 21, 396
- Jarrett, T. H. 2000, *PASP*, 112, 1008
- Jarrett, T.-H., Chester, T., Cutri, R., Schneider, S., Rosenberg, J., Huchra, J. P., & Mader, J. 2000a, *AJ*, 120, 298
- Jarrett, T. H., Chester, T., Cutri, R., Schneider, S., Skrutskie, M., & Huchra, J. P. 2000b, *AJ*, 119, 2498
- Karttunen, H., Kroeger, P., Oja, H., Poutanen, M., & Donner, K. J. 2003, *Fundamental Astronomy* (Springer)
- Kerr, F. J. & Henning, P. A. 1987, *ApJ*, 320, L99
- Kirby, E. M., Jerjen, H., Ryder, S. D., & Driver, S. P. 2008, *AJ*, 136, 1866
- Kochanek, C. S., Pahre, M. A., Falco, E. E., Huchra, J. P., Mader, J., Jarrett, T. H., Chester, T., Cutri, R., & Schneider, S. E. 2001, *ApJ*, 560, 566
- Kogut, A., Lineweaver, C., Smoot, G. F., Bennett, C. L., Banday, A., Boggess, N. W., Cheng, E. S., de Amici, G., et al. 1993, *ApJ*, 419, 1
- Kraan-Korteweg, R. C. 2000, *A&AS*, 141, 123
- Kraan-Korteweg, R. C. 2005, in *Reviews in Modern Astronomy*, Vol. 18, *Reviews in Modern Astronomy*, ed. S. Röser, 48–75
- Kraan-Korteweg, R. C. & Lahav, O. 2000, *A&A Rev.*, 10, 211
- Landowitz, L. F. & Marshall, L. 1960, *Nature*, 187
- Masters, K. L., Giovanelli, R., & Haynes, M. P. 2003, *ApJ*, 126, 158
- Meyer, M. J., Zwaan, M. A., Webster, R. L., Staveley-Smith, L., Ryan-Weber, E., Drinkwater, M. J., Barnes, D. G., Howlett, M., et al. 2004, *MNRAS*, 350, 1195
- Möllenhoff, C. & Heidt, J. 2001, *A&A*, 368, 16
- Nagashima, C., Nagayama, T., Nakajima, Y., Tamura, M., Sugitani, K., Nagata, T., Hirao, T., Nakaya, H., Yanagisawa, K., & Sato, S. 1999, in *Proceedings of Star Formation*, ed. T. Nakamoto, 397–398

- Nagayama, T., Nagashima, C., Nakajima, Y., Nagata, T., Sato, S., Nakaya, H., Yamamuro, T., Sugitani, K., & Tamura, M. 2003, in *Instrument Design and Performance for Optical/Infrared Ground-based Telescopes (SPIE)*, ed. M. Iye & A. F. M. Moorwood, Vol. 4841, 459–464
- Nakajima, Y., Kandori, R., Tamura, M., Naoi, T., Nagata, T., Nagayama, T., Kato, D., & Sugitani, K. 2008, *PASP*
- Oke, J. B. & Sandage, A. 1968, *ApJ*, 154, 21
- Poggianti, B. M. 1997, *A&AS*, 122, 399
- Saunders, W., d’Mellow, K. J., Tully, R. B., Mobasher, B., Carrasco, B. E., Maddox, S. J., Hau, G. K. T., Sutherland, W. J., et al. 2000a, in *ASP*, Vol. 218, *Mapping the Hidden Universe: The Universe behind the Milky Way - The Universe in HI*, ed. R. C. Kraan-Korteweg, P. A. Henning, & H. Andernach, 153
- Saunders, W., Sutherland, W. J., Maddox, S. J., Keeble, O., Oliver, S. J., Rowan-Robinson, M., McMahon, R. G., Efstathiou, G. P., et al. 2000b, *MNRAS*, 317, 55
- Schechter, P. 1997, *ApJ*, 203, 297
- Schlegel, D. J., Finkbeiner, D. P., & Davis, M. 1998, *ApJ*, 500, 525
- Schröder, A., Kraan-Korteweg, R. C., Mamon, G. A., & Ruphy, S. 1997, in *Extragalactic Astronomy in the Infrared*, ed. G. A. Mamon, T. X. Thuan, & J. Tran Thanh van, 381
- Schröder, A. C., Kraan-Korteweg, R. C., Mamon, G. A., & Woudt, P. A. 2005, in *Astronomical Society of the Pacific Conference Series*, Vol. 329, *Nearby Large-Scale Structures and the Zone of Avoidance*, ed. A. P. Fairall & P. A. Woudt, 167
- Shafi, N. 2008, Master’s thesis, University of Cape Town
- Silva, L., Granato, G. L., Bressan, A., & Danese, L. 1998, *AJ*, 509, 103
- Staveley-Smith, L., Juraszek, S., Koribalski, B. S., Ekers, R. D., Green, A. J., Haynes, R. F., Henning, P. A., Kesteven, M. J., et al. 1998, *AJ*, 116, 2717
- Staveley-Smith, L., Wilson, W. E., Bird, T. S., Disney, M. J., Ekers, R. D., Freeman, K. C., Haynes, R. F., Sinclair, M. W., et al. 1996, *Publications of the Astronomical Society of Australia*, 13, 243
- Strutskie, M. F. 2006, *AJ*, 131, 1163
- Tinsley, B. M. 1980, *ApJ*, 241, 41
- Wakamatsu, K., Hasegawa, T., Karoji, H., Sekiguchi, K., Menzies, J. W., & Malkan, M. 1994, in *Astronomical Society of the Pacific Conference Series*, Vol. 67, *Unveiling Large-Scale Structures Behind the Milky Way*, ed. C. Balkowski & R. C. Kraan-Korteweg, 131

Wong, O. I., Ryan-Weber, E. V., Garcia-Appadoo, D. A., Webster, R. L., Staveley-Smith, L., Zwaan, M. A., Meyer, M. J., Barnes, D. G., et al. 2006, MNRAS, 371, 1855